LUND UNIVERSITY

Artificial protein molecular motors and fluorescence enhancement in nanowires for biosensing

Unksov, Ivan

2023

Document Version:
Publisher's PDF, also known as Version of record

[Link to publication](#)

Total number of authors:
1

Artificial protein molecular motors and fluorescence enhancement in nanowires for biosensing

IVAN N. UNKSOV

DIVISION OF SOLID STATE PHYSICS | FACULTY OF ENGINEERING | LUND UNIVERSITY

Artificial protein molecular motors and fluorescence enhancement in nanowires for biosensing

Artificial protein molecular motors and fluorescence enhancement in nanowires for biosensing

Ivan N. Unksov

LUND
UNIVERSITY

Organization: LUND UNIVERSITY

Document name: Doctoral Dissertation   **Date of issue:** Oct 6

Author(s):   Ivan N. Unksov   **Sponsoring organization:**

Title and subtitle: Artificial protein molecular motors and fluorescence enhancement in nanowires for biosensing

Abstract:

Artificial molecular motors are an ambitious attempt to mimic and surpass natural motors, one of the most fascinating entities in the molecular realm. Once developed, artificial constructs require characterization of their performance. The types of motors developed to date and methods (optical and electron microscopy, FRET, force measurements) to characterize their motion are outlined in the review (Paper I) included in this thesis.

In the first project of the thesis, novel synthetic protein-based molecular motors are characterised using optical microscopy. We study their interaction with tracks, development of which was another goal of this work. For one construct, the Lawnmower, the motion is achieved and tracked in selectively functionalised microchannels, and the extent of superdiffusive motor activity is analysed. This motor is capable of autonomous motion, harnessing the diffusion without a supply of any external reagents. Another design, the Tumbleweed, is a single-molecule protein motor synthesised to bind to and move along a DNA track in a controllable manner. This work lies ground for still ongoing experiments on observing its motion along a DNA track by optimising surface chemistry and developing double-stranded and DNA origami tracks for single-molecule FRET.

For molecular motors and other molecular objects, detection in solution at a single-molecule level is an important challenge. The second project of this thesis is a study of the optical biosensing capabilities of semiconductor nanowires. Fluorescence enhancement by semiconductor nanowires is investigated, including contributions from excitation enhancement and Purcell emission enhancement. For quantifying the excitation, photobleaching rate measurements are used to find a range of diameters that maximize the enhancement. Compared to this effect, a study of emission modification by fluorescence lifetime measurements do not show a pronounced influence of the nanowires but is nevertheless illustrative. These results are further utilized in an original design of a biosensor for detection of label-free DNA, which harnesses the nanowires and fluorescent DNA-templated silver nanoclusters.

In the future, nanowires may be used for molecular motor studies, for which the reported development of tracks based on DNA and surface functionalization is also relevant. This thesis links these results, puts them in the context of their respective fields of knowledge and provides an outlook on potential advances of artificial molecular motors and nanowire biosensors.

Keywords:

Molecular motors, nanowires, fluorescence, biosensors

Recipient's notes   **Number of pages**:61

Price   Security classification

Signature   Date 2022-08-21

Artificial protein molecular motors and fluorescence enhancement in nanowires for biosensing

Ivan N. Unksov

We all seek miracles, Sphinx. Some miracles are feasible, and some are not, so we choose what is possible.

— Mariam Petrosyan, The Grey House

'According to my calculations, the comet will reach the Earth on October the 7th at 20.42 or perhaps 4 seconds later,' Professor replied. 'And what happens then?' Sniff inquired. 'What happens?' Professor looked puzzled, 'Have never thought about that. But, in any case, I will report it in detail.'

— Tove Jansson, Comet in Moominland

To my parents

Table of Contents

Abstract

Artificial molecular motors are an ambitious attempt to mimic and surpass natural motors, one of the most fascinating entities in the molecular realm. Once developed, artificial constructs require characterization of their performance. The types of motors developed to date and methods (optical and electron microscopy, FRET, force measurements) to characterize their motion are outlined in the review (Paper I) included in this thesis.

In the first project of the thesis, novel synthetic protein-based molecular motors are characterised using optical microscopy. We study their interaction with tracks, development of which was another goal of this work. For one construct, the Lawnmower, the motion is achieved and tracked in selectively functionalised microchannels, and the extent of superdiffusive motor activity is analysed. This motor is capable of autonomous motion, harnessing the diffusion without a supply of any external reagents. Another design, the Tumbleweed, is a single-molecule protein motor synthesised to bind to and move along a DNA track in a controllable manner. This work lies ground for still ongoing experiments on observing its motion along a DNA track by optimising surface chemistry and developing double-stranded and DNA origami tracks for single-molecule FRET.

For molecular motors and other molecular objects, detection in solution at a single-molecule level is an important challenge. The second project of this thesis is a study of the optical biosensing capabilities of semiconductor nanowires. Fluorescence enhancement by semiconductor nanowires is investigated, including contributions from excitation enhancement and Purcell emission enhancement. For quantifying the excitation, photobleaching rate measurements are used to find a range of diameters that maximize the enhancement. Compared to this effect, a study of emission modification by fluorescence lifetime measurements do not show a pronounced influence of the nanowires but is nevertheless illustrative. These results are further utilized in an original design of a biosensor for detection of label-free DNA, which harnesses the nanowires and fluorescent DNA-templated silver nanoclusters.

In the future, nanowires may be used for molecular motor studies, for which the reported development of tracks based on DNA and surface functionalization is also relevant. This thesis links these results, puts them in the context of their respective fields of knowledge and provides an outlook on potential advances of artificial molecular motors and nanowire biosensors.

Acknowledgements

The molecular motors in this thesis may be an illustration to the Dao De Jing's famous '*A journey of a thousand miles begins with a single step*', although those are more like nano- or micromiles here. Anyway, the journey of my PhD became walkable thanks to many people to whom I would like to express my gratitude.

The first one goes to Heiner, my supervisor (or *surevisor*, a not entirely incorrect typo I made a couple of times in my writing). Thank you for the ambitious projects you offered me in this PhD. Thank you for the freedom and, at the same time, the support you gave me in working on my things. And thank you for the time you were tearing from your busy schedule whenever I *really* needed help in my projects but even more so in my life. Sorry if the bike was heavy but the chandelier still serves me well. Finally, thanks for bringing awesome people from around the world into your group. Of whom below...

Pradheebha, Ruby, Palle, Julia, Michael, Gerda, you were extraordinary, within the walls of FTF but in many cases also outside. It has been an experience to get to know you, and thank you for bearing with a not very social me. Now Mikkel and Nils have boarded, and I hope we will have some great time together while I am still around. To the former Linke group – Mariia, Jingyuan, Roman, Jonatan, Damiano, Frida, Zeus − if you read this, it was a pleasure to meet you.

Thank you, Sara, for being my co-supervisor. Although we have worked together only shortly, it is to that time I owe most of what I know about proteins.

A big part of my work was taming the Lawnmower motors with Nancy Forde and Chapin Korosec. Although I have not had a chance to meet you in person, together we really pushed it through, thank you for your dedication and drive.

Thanks to Paul Curmi and all Tumbleweed-growers, I tasted many mangos and took some dips in Sydney. It has been interesting to participate in this unique project, and I hope Tumbleweed will stand up confidently on its feet soon.

On the planet of Lund Kemicentrum, I learned a bunch of things in the Peter Jönsson and Ivan Scheblykin groups. Special thanks is to Tommy, you were so unselfishly helpful so many times.

Some nanowire platforms I used in the nanocluster project were generously provided by AlignedBio AB whom I would also like to thank for interesting discussions.

For gearing all the work, I am grateful to the amazing people of FTF. Bengt, Anders, Natalia, Peter, Alex, Alfons, Andreas and others, without you the cleanroom and computers would not have lasted long if at all. And administration relentlessly carried out by Marica, Anna-Karin, Alexandra, Mirja and all, made FTF feel like home (including all the yummy cakes).

Thanks to the Biogroup people for our Friday meetings, sometimes entertaining and sometimes bringing good advice. The time among you Biowasters was definitely not wasted.

To all FTF and NanoLund folks, I say thank you all for your help and fun we had together during lunches, fikas, retreats and at numerous other times. And particularly to other PhD students: they say we are not as cool as 'real' students, but I argue some of the latter would envy how many things we were up to.

Marina, your help in proofreading this entire thing was offered magically just in time when I needed it. I hope it will soon be my turn to read yours. And thank you for checking on me regularly through all these years, with the German punctuality that they say exists.

My time in Sweden would simply not happen without the support of my parents and friends. In the often dark times, you have been a God-given guiding light for me.

<div align="right">
Vanya Unksov

Lund, August 2023
</div>

Popular science summary

Biological molecules are the tool by which Nature operates. One astonishing example is molecular motors. These molecules harvest energy from their environment, often from chemical interactions with other molecules, and use it to propel themselves, just like a motor in one's car uses fuel or electricity. Natural molecular motors are responsible for many functions in our cells, including muscle contraction and transport of reagents. Nature's motor molecules are proteins, that is, they belong to one of the major classes of molecules that define the living matter. Natural motors can move extremely fast, covering up to tens of micrometers (1 micrometer is 1/1 000 000 of a meter) per second, and this distance is 100-1000 times larger than their size. Reaching a comparable performance is an ambitious aim of creating artificial molecular motors, that is, motile synthetic constructs. Artificial motors would not only allow for a wider range of applications than their natural counterparts but also would help understand the motion of natural motors.

Here, we study two artificial motors whose common feature is that they are made of proteins that are not motors by themselves but can achieve motor functionality when assembled in larger constructs. One of them, nicknamed the Lawnmower, is a micrometer-sized bead that moves owing to many molecules on its surface (**Figure 1**A). These molecules are enzymes, which means that they have a specific biological activity. In our case, they cleave other molecules forming the 'lawn' for the motor (hence the name). When the lawn has been cleaved, the enzymes are searching for and reaching a fresh patch, and this search drives the motor. To better control the direction of their motion, we made channel-like tracks (also micrometer-sized). In these tracks, we characterize the motion by observing it with a microscope and tracking the Lawnmowers.

The other motor is dubbed Tumbleweed and designed to operate truly as a single molecule (**Figure 1**B). It is made of three smaller proteins that bind to a long molecule of DNA, another major type of biological molecules. For the Tumbleweed, the long strand of DNA serves as a track which can be made of a desired length, defining how many steps the motor will be able to take. Another control here is the motor's surroundings: to bind to the DNA track, Tumbleweed needs external helper molecules called ligands. Thus, one controls the motion of Tumbleweed by regulating the supply of the ligands. Once a ligand has been changed, one foot detaches from the DNA but another foot remains bound, and the motor takes a step. Such an intricate system suffers when the motors bind not to the designated parts of the DNA track but, for example, to the surface where the track is mounted. In this work, we test several approaches to minimize non-specific binding. By using a microscope, we are able to see individual motors, as they are fluorescently labelled. That means that each motor is chemically linked to one or several small molecules which are fluorescent, that is, shine back light (emission) when there is incoming light (excitation) of a higher energy.
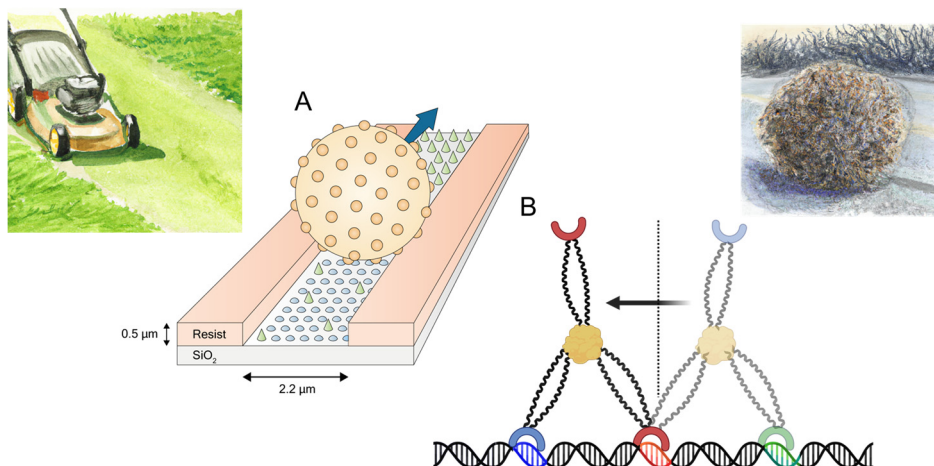
Figure 1. Artificial protein-based molecular motors. (A) Lawnmower, enzymes on the bead depicted as yellow semi-spheres, and the lawn as green cones. Adapted from the Paper II. (B) Tumbleweed, DNA-binding components and their binding sites on the DNA are depicted in green, red and blue respectively.

One way towards more sensitive detection of fluorescent molecules, including the motors in motion, is to enhance the fluorescence. Semiconductor nanowires are elongated objects with a diameter of tens to hundreds of nanometers (1 nanometer is $1/10^9$ of a meter) and length of a few micrometers. Due to optical resonances, they enhance the signal of fluorophores in their proximity, additionally serving as optical fibers that guide the signal. A surface with many nanowires on it also provides a high throughput of detection from each image taken at an optical microscope. However, the physics of fluorescence enhancement and its dependence on the nanowire geometry must be understood. Therefore, the second part of this work is about fluorescence in proximity of semiconductor nanowires. We find that diameters of 90-130 nm provide the best signal enhancement for red fluorophores, with excitation over five times stronger than in the rest of the solution.

We use these results to detect short DNAs in solution, which may find a medical application. For this, we designed a sensor where the nanowires enhance the fluorescence of DNA-templated silver nanoclusters, and their fluorescence additionally increases in presence of the target DNA. Besides this application, we provide an outlook on how the nanowires can be used for characterization of our molecular motors.

14

List of Papers

Paper I

Unksov, I.N.; Korosec, C.S.; Surendiran, P.; Verardo, D.; Lyttleton, R.; Forde, N.R.; Linke, H. Through the Eyes of Creators: Observing Artificial Molecular Motors. *ACS Nanoscience Au* **2022**, doi:10.1021/acsnanoscienceau.1c00041.

I conceived the study together with co-authors, I planned and performed the experiments and analysis of the Lawnmower motion in quasi-1D channels (Section 4.1). Most of the paper is a review but it also includes original results. I performed the literature review, wrote the review sections and the section on original results from Lawnmower experiments in microchannels, whereas other sections with original results were contributed by co-authors.

Paper II

Korosec, S.*; Unksov, I.N.*; Surendiran, P.; Lyttleton, R.; Curmi, P.M.G.; Angstmann, C.N.; Eichhorn, R.; Linke, H.; Forde, N.R. The Lawnmower: An Autonomous, Protein-Based Artificial Molecular Motor. *Under revision for Nature Communications*. Preprint: https://arxiv.org/ftp/arxiv/papers/2109/2109.10293.pdf

* These authors contributed equally.

I conceived the study together with co-authors, performed the experiments, and participated in the further analysis of the Lawnmower motion in quasi-1D channels. I contributed to discussion and writing as a shared first author.

Paper III

Unksov, I.N.; Anttu, N.; Verardo, D.; Höök, F.; Prinz, C.N.; Linke, H. Fluorescence Excitation Enhancement by Waveguiding Nanowires. *Nanoscale Adv* **2023**, 1–7, doi:10.1039/d2na00749e.

I conceived the study together with coauthors, performed experiments and analysed the data. I wrote the paper with input from all authors.

Paper IV

Unksov, I.N.; Davtyan, R.; Höök, F.; Linke, H. Biosensor for Short DNA Based on Fluorescent Silver Nanoclusters and Semiconductor Nanowires. *In Prep.*

I suggested the idea and realisation of the study, participated in experiments and analysis, and wrote the manuscript with editing provided by co-authors.

Abbreviations

AFM	Atomic Force Microscopy
ALD	Atomic Layer Deposition
BSA	Bovine Serum Albumin
FIONA	Fluorescence Imaging with One-Nanometer Accuracy
FRET	Förster Resonance Energy Transfer
LM	Lawnmower (molecular motor)
NA	Numerical Aperture
NCs	Nanoclusters
NWs	Nanowires
PBS	Phosphate-buffered Saline
SEM	Scanning Electron Microscopy
SPR	Surface Plasmon Resonance
TIRF microscopy	Total Internal Reflection Fluorescence microscopy
TW	Tumbleweed (molecular motor)

1 Introduction

Molecular motors are natural and artificial constructs that perform motion owing to a source of energy that can be thermal, chemical, photons or electrons. This energy is not converted into heat as in macroscopic thermodynamic engines. Many natural motors have high energy efficiencies, e.g., $40-60\%$ for kinesins when defined as $\eta = F\delta/\Delta G$ where the upper part is the work against the external mechanical force F for a step size δ, and ΔG is the free energy.[1] For comparison, a gasoline car engine has a practical efficiency of $20-40\%$. Additionally, natural motors are fast (Figure 2) and processive (i.e. can stay on the track for a prolonged time).

Inspired by the natural motors, many artificial constructs have been designed. One motivation is to better understand how natural motors create energy-dependent asymmetry, that is, a minimum of free energy corresponding to one direction, for high-speed directional motion that to the date remains unsurpassed by artificial motors. Another reason for these efforts are potential applications where future artificial motors may be more controllable that natural counterparts. These include cargo transportation,[2,3] switches and rotors,[4–7] photoswitchable systems to record digital information,[8] few-atom sized machines employing quantum tunnelling for directional motion,[9] motors for photothermal therapy of cancer,[10] formation of motile supramolecular assemblies,[11] manipulations with cells.[12]

In this work, we develop polyvalent artificial motors, that is, the ones with more than two functional 'legs', each capable of binding to a substrate (Figures 1-3). Polyvalent constructs are among the key types of the synthetic motors alongside those based on molecular isomerization explored particularly by Feringa and co-workers,[13] and DNA walkers utilising hybridization with a DNA track.[14–17] With a varied number of legs, polyvalent motors are particularly interesting as they can be both supramolecular assembles and single molecules, ranging in scale from the nano- to micro-. Of notable recent designs are the motors based on nanoparticles and DNA origami by Salaita and co-workers.[18–21] Polyvalency is a source of asymmetry, that is, the legs bound to the substrate define the spatial orientation of a motor and accessibility of the substrate for the legs not bound. However, it also presents a challenge as binding and dissociation of the legs must be coordinated to avoid motors being stuck or falling off the track.
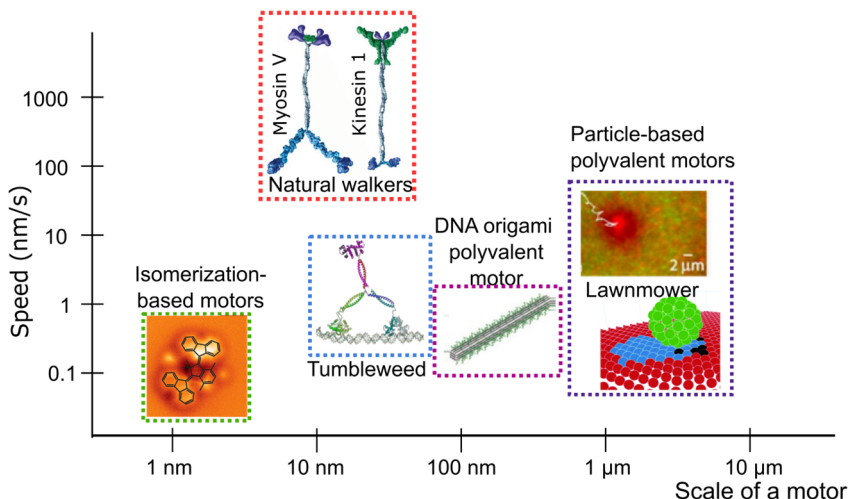
Figure 2. Exemplary size and speed of synthetic molecular motors as compared to natural motors. Synthetic motors are diverse in size, however their natural counterparts are superior in speed. The Tumbleweed and Lawnmower motors are part of this thesis. For natural motors speeds are based on Refs. [22–25], for isomerization motor on Ref. [26], for DNA origami motor on Ref. [18], for particle-based motors on Refs. [19–21,27,28]. Image of the isomerisation-based motor is reproduced from Ref. [26]. Copyright 2023 American Chemical Society. Protein walker adapted from Ref. [29]. Copyright 2017 American Chemical Society. DNA origami motor adapted from Ref. [18] with permission from John Wiley and Sons. Copyright 2020. One of bead motor (bottom) reproduced from Ref. [28] with permission. Copyright 2020 Royal Society of Chemistry. Another bead motor (top) reprinted from Ref. [30] with permission from PNAS. Natural motors adapted from Ref. with permission from Elsevier. Copyright 2003.

To date artificial molecular motors have been largely based on nucleic acid hybridization and isomerization of non-biological molecules. Using proteins in the motors would instead employ a variety of interactions between proteins, nucleic acids and small molecules. This toolbox of protein chemistry has not been employed in motor designs, while it has unique features: protein binding in many cases is highly specific, reversible, or allosteric.

In this work, we study two protein-based motors, nicknamed the Lawnmower (LM) and Tumbleweed (TW). The Lawnmower, described in detail in Section 3.3, was originally introduced in Ref. [31] and is built on a hub to which proteases are attached. On a peptide-coated 'lawn' surface, protease activity of these 'blades' biases otherwise diffusive motion of the hub (**Figure 3**A). Resulting motion is expected to be autonomous, that is, the motor relies on lawn cleavage and diffusion, not on externally supplied reagents or stimuli; this feature is unique to date. In the pioneering study[31], trypsin molecules were attached to a quantum dot, and the resulting construct was shown to cleave peptides in solution. In Papers I and II, we implemented a Lawnmower that presents a development of that concept but built on

a microsphere that allows for a polyvalency of 5 orders of magnitude larger than a quantum dot. Higher polyvalency, in turn, has been predicted to increase force generated by a motor[32] and its processivity[33], that is, it does not detach from the track for longer.

Natural molecular motors are typically moving along a track. This has been used for biosensing[34] and energy efficient biocomputation[35,36]. Our motivation has therefore been to achieve Lawnmower motion using a channel. In Papers I-II, we achieved this in microfabricated channels (**Figure 3**B), and assessed the extent to which the motion is superdiffusive, that is, the displacement of a motor grows over time t as t^α where for superdiffusive motion $1 < \alpha < 2$.
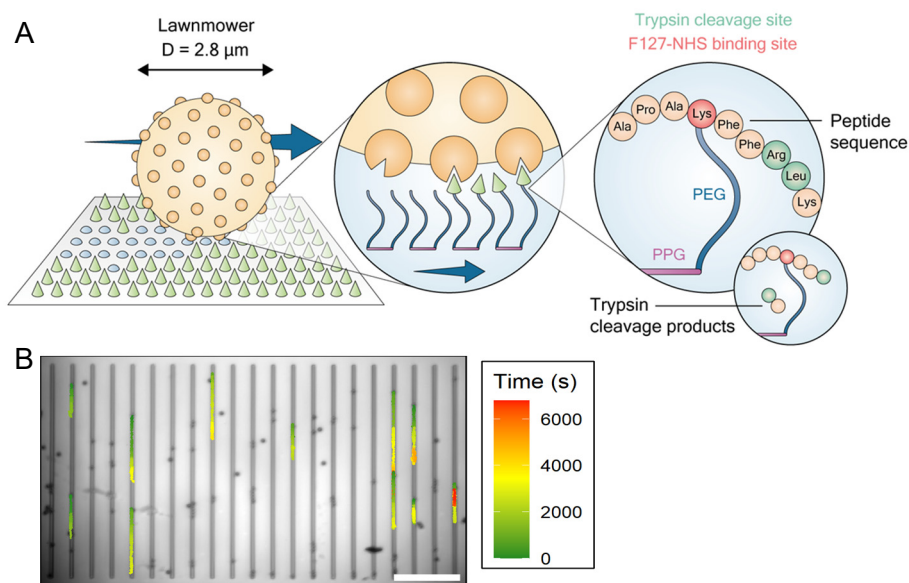
Figure 3. The Lawnmower motor. (A) Trypsins on a microsphere cleave the peptide lawn. (B) Motors (dark spots) move along the channels where the lawn is selectively deposited on the bottom. Many motors remain stuck. Scale bar is 50 μm. Adapted from the Paper II.

Unlike the microsphere Lawnmower, the Tumbleweed is a nanosized motor, designed to bind to and move along a DNA track (**Figure 4**). Its concept[37] pioneers *de novo* design of a molecular motor from non-motor proteins. Site-specific binding of protein repressors to DNA is dependent upon ligands, thus sequential switching of buffers allows stepping of the motor along the track in steps as small as 10-15 nm. By itself, double stranded synthetic DNA is a robust polymer with a relatively

large persistence length of ~50 nm, which makes it an attractive track for molecular motors. Since the original concept[37], a number of designs for the motor and tracks has been tested in our laboratory and by co-workers. However, the evidence of its stepping has not yet been accomplished, due to challenges of observing the small steps and of unspecific binding. This work lays the ground for the observation by developing surface passivation, as well as FRET and surface optical profilometry approaches to study the TWs. Finally, we developed 400 nm-long DNA origami nanotube tracks for the TW. All these are described in Section 3.5.
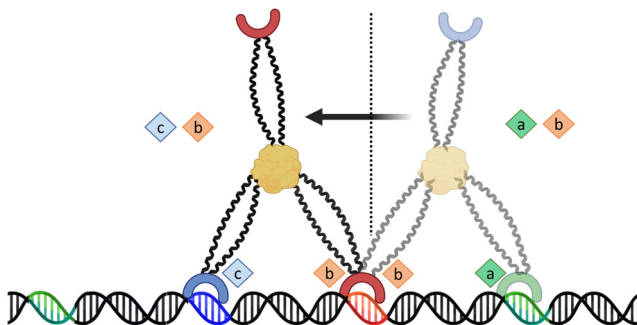
Figure 4. The Tumbleweed molecular motor on a DNA track. TrpR, DtxR and MetJ repressors are depicted in green, red and blue respectively; same colours are used for the corresponding binding sites on the DNA, and the ligands that enable binding. The motor takes a step when the ligand pair (a, b) is replaced with (b, c).

Observation of single fluorescent molecules, including Tumbleweed, has obstacles such as poor signal-to-noise ratio and diffraction limit of an optical microscope. Unique properties of nanowires (NWs) made of some semiconductor materials with a high refractive index include local enhancement of fluorescence and lightguiding. These make the NWs promising in single-molecule fluorescence microscopy, as well as for biosensors based on fluorescence. NWs are elongated structures fabricated with high surface-to-volume ratio (see Section 4.1 for the details). In the NWs, optical resonances correspond to waveguide modes, to which fluorescence of the neighbouring fluorophores can be coupled and by which it is enhanced and guided. The second part of this thesis overarches fluorescence enhancement in GaP (gallium phosphide, III-V semiconductor with a refractive index > 3.1 for visible light) nanowires and use of this effect for fluorescence-based biosensing. These are Papers III and IV.

The fluorescence enhancement has been previously shown for NWs and similar elongated structures of semiconductor materials such as ZnO[38,39], GaP[40,41], Si[42,43], InAs[44] and GaAs[45,46]. It found applications for biomolecular systems, typically where the molecules were labelled with a fluorescent dye. ZnO NWs and similar nanorods have been particularly widely used in that paradigm, including detection

of human α-fetoprotein[47] and carcinoembryonic antigen[47,48], several biomarkers[49], and SARS-CoV-2 nucleocapsid[50] proteins. In several studies[49,50], the achieved sensitivity surpassed that of enzyme-linked immunosorbent assays (ELISA).

We study GaP NWs that have been employed less extensively, however have valuable properties. A high refractive index of GaP allows waveguiding and enhancement of fluorescence. Additionally, low absorbance of visible light reduces losses of the signal, as well as photoluminescence of the NWs in absence of external fluorophores. Apart from quantitative characterization of GaP NWs as fluorescence enhancers for a range of NW diameters and lengths, we seek to investigate the phenomena behind the fluorescence enhancement.

In Paper III, we study enhancement of excitation, a phenomenon majorly contributing to the overall signal enhancement. This study covers a range of NW diameters and excitation wavelengths, determining the optimal ranges. Using time-resolved microscopy, we additionally estimate Purcell emission enhancement by the NWs. This compliments the other studies carried out in our laboratory, where GaP NWs of selected diameters have been shown to enhance the overall signal 10-200-fold compared to fluorophores bound to a planar surface[41], and enable efficient waveguiding[51].
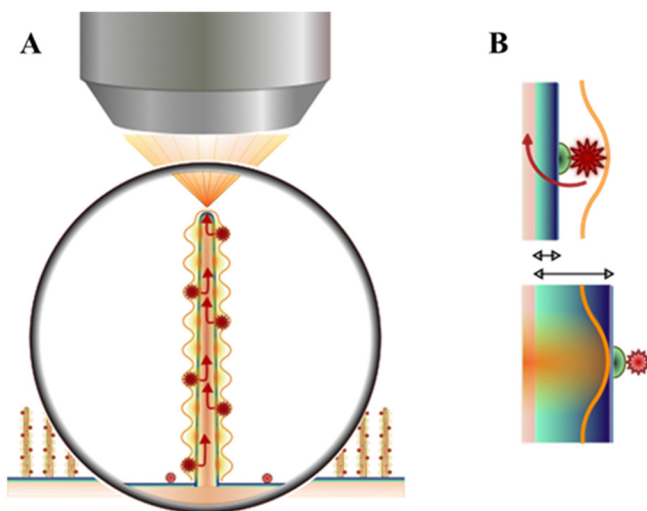
Figure 5. Fluorescence enhancement and lightguiding in NWs. (A) Excitation and emission of fluorophores in proximity of a NW is enhanced and guided by the NW. (B) Excitation enhancement decreases with distance from the nanowires, defined by an oxide coating. Adapted from the Paper III with permission. Copyright 2023 Royal Society of Chemistry.

NW-based detection of self-assembling fluorescent systems in low concentrations is especially interesting. In Paper IV, we use the knowledge about optimal NW

dimensions in a biosensor for label-free optical detection of DNA in solution. For that, we combine NWs with DNA-templated silver nanoclusters (NCs) that exhibit label-free fluorescence ranging from green to near-IR;[52,53] for details of the NCs behaviour, see Section 5.1. A unique feature of NCs is that the fluorescence is significantly increased when a NC-templating DNA strands encounters a guanine-rich strand[53], which is attributed[54,55] to a high binding affinity between Ag^+ and guanine. This enables nanocluster beacons, biosensors pioneered in Refs.[53,56], where a target DNA brings together the two strands in a junction construct. However, these studies were performed in bulk, except for detection of ATP using silver NCs that has been realized[57] on ZnO nanorods.

As opposed to detection in bulk solution, present a nanocluster beacon (Paper IV and Section 5) where the signal of NCs is enhanced by NWs as it binds to the oxide layer on the NWs. Sensitivity of the biosensor is increased as the signal is multiplexed by many NWs within a field of view of a microscope and due to the fluorescence enhancement. We envision the application of this design in customisable detection of short DNAs or RNAs. Such systems can be more cost-effective compared to those involving organic fluorophores, and beacons with different colour and/or target can be combined in one biosensor.
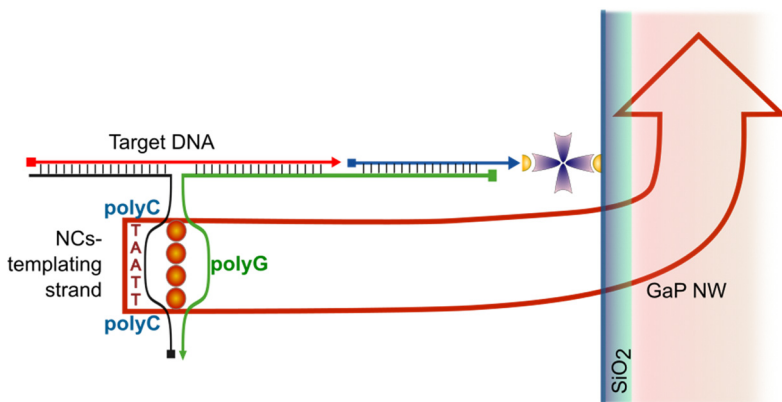
Figure 6. Nanocluster beacon assembles on an oxide coating of a GaP NW only in presence of a target DNA that brings together the NCs templating and G-rich strands. Fluorescence is enhanced by the NW, coupled into it, and guided. Adopted from the manuscript Paper IV.

To summarise, this work uses optical microscopy for characterization of novel molecular motors and for development of NW platforms that can be used for detection of low amounts of fluorescent molecules. We developed tracks and observation strategies for two synthetic molecular motors. For the NWs, we found the dimensions that maximise fluorescence enhancement and showed how this enhancement depends on a distance from the NW. We then combined the optimized

nanowires with DNA-templated nanoclusters in a biosensor for cost-efficient detection of DNA that has a potential to be used also for RNA.

Beyond these questions, more ideas can be implemented in future studies. As the NWs enhance and guide fluorescence only locally, in 50−100 nm proximity of their surface, they can be employed to detect sub-diffraction movements of fluorescent molecular motors such as TWs that would move towards or from a NW. In such experiments, the DNA tracks could be labelled with a variety of fluorescent nanoclusters if the track incorporates the sequences to anchor those. In case many positions need to be labelled, e.g. multiple different staple strands of a DNA nanotube, nanoclusters can massively reduce the costs compared to oligonucleotides with organic fluorophores. Furthermore, a variety of other systems with biosensing capabilities can be combined with the NWs, such as DNA aptamers and hairpins.

Another pathway for NW-based detection for the motors such as LMs that change their substrate when visiting a location, is to make that substrate fluorogenic. Once assembled on NWs, it would highlight the activity of the motor, enhancing the fluorescence. As reviewed in the Paper I, this has been previously attempted for the LMs and GaP NWs. This and other perspective experiments are described in more detail in the Outlook section of this thesis.

2 Optical microscopy and fluorescence

Optical microscopy features high temporal resolution (typically, down to tens of ms) and allows to study samples in solution. These factors make it a method of choice for many studies on molecular objects, including this work. However, conventional optical microscopy is limited by diffraction, i.e. it presents an object, no matter how small, as a point-spread function. This is described as an Airy disk of the radius given by

$$r_A = \frac{0.61\lambda}{\text{NA}} \tag{1}$$

where λ is the wavelength of the light used for observation, and NA is the numerical aperture of the objective. The radius (1) also limits the distance between several objects that are resolved. For visible wavelengths, the resolution limit is a few hundred nm. To see NWs that are smaller than the resolution limit, we use SEM, and AFM to observe DNA nanotubes. However, these methods are not an option for our molecular motors in solution.

Microscopy modalities are reviewed in the context of motor experiments in the Paper I. The samples in microscopy experiments are often fluorescent, although there exist also label-free microscopy techniques, e.g., brightfield (the image is formed by illumination transmitted through the sample) and darkfield (the image is formed by scattered light) microscopy. In this work, we used fluorescence microscopy to observe fluorophores on nanowires (NWs) (Papers III-IV), and fluorescently labelled TW motors (Section 3.5). For the LM motors, opaque particles with a 2.8 μm diameter moving on non-transparent reflective SiO_2, we did imaging with ambient illumination.

With their diameters of 50−200 nm, NWs fall behind the diffraction limit. For that reason, we acquired the fluorescence from diffraction-limited spots around the NWs, excluding close standing multiple NWs that yield a non-circular PSF.

For time-resolved measurements on NWs, we also used a microscope. This setup had an APD (avalanche photodiode) detector, and the size of the region of interest around individual NWs was taken as small as possible (< 1 μm) to minimize the influence of the background.

For imaging single TWs (Section 3.5), we used objective-based TIRF, an improvement of conventional optical microscopy that increases signal-to-noise ratio, as the primary excitation light is reflected as $\theta_c < \theta < \alpha$, where θ_c is the critical angle of total internal reflection, θ is the angle feasible for the TIRF objective, and $\alpha = \arcsin\left(\frac{\mathrm{NA}}{n}\right)$ for an immersion media with refractive index n (we used an oil immersion NA = 1.49 60x objective (Nikon). This light induces evanescent waves that are the only source of excitation in the sample. The evanescent excitation decays exponentially within a hundred nm in the sample. This prevents the rest of the sample from excitation, thus minimizing the background signal.

However, TWs also fall behind the diffraction limit, being as small as about 25-30 nm. To observe their steps, we use the TIRF setup in a FRET (Förster Resonance Energy Transfer) experiments. The FRET efficiency is inversely proportional to $1 + \left(\frac{r}{R}\right)^6$, where r – the distance in a FRET pair, R – 50 % efficiency distance[58]. That stems from a spectral overlap between donor and acceptor; a larger overlap increases the distance[59] but also parasitic signal bleeding through the emission filters. We used AlexaFlour 488 as a donor on the TrpR foot of TW and a corresponding site of the DNA was bearing an acceptor ATTO565; this pair has $R = 6.4$ nm so FRET is expected to be lost upon the detachment of the foot (see 3.5 for more details).

In future, it is interesting to study nanosized molecular motors such as TWs, using super-resolution techniques or localisation microscopy (FIONA approach[60,61]). These perspective experiments are discussed in the Outlook.

3 Molecular motors

3.1 Why do molecular motors move?

In this work, synthetic motors move along their substrate. This walking motion is opposed to rotation of isomerization-based motors or motion of microswimmers. The motor motion requires the negative change in free energy ($\Delta G < 0$) and a non-equilibrium system. Two loosely defined manners in which artificial and natural walker motors may operate are Brownian ratchets and power stroke.

Brownian ratchets move at non-equilibrium conditions by rectifying diffusion through asymmetry in the free energy landscape. This can be done by releasing free energy when converting the visited substrate into a product that is unfavourable for repeated binding of the motor, which makes a certain direction beneficial for their motion (so called burnt-bridges motor).

The second mechanism, power stroke, implies that the energy harvested by a motor is used for a conformational change in the motor, which in turn causes directionality.[62] One finds examples of the power stroke in natural molecular walkers: ATP hydrolysis in kinesins is followed by a conformational change in the neck linker region,[63] and myosin motion involves rotation of an elongated α-helix arm that serves as a rigid lever.[62] These natural motors are highly efficient: when defined as $\eta = F\delta/\Delta G$ where the upper part is the work against the external mechanical force F for a step size δ, and ΔG is the free energy, the efficiency reaches 40% for myosin and 60% for kinesin.[1] The forces here are on pN scale and can be compared to the thermal energy at room temperature $kT \approx 4$ pN nm. Reconstruction of the above principles in a synthetic system drives the creation of artificial motors.

3.2 Materials to build an artificial motor

A popular material for artificial walker motors is DNA. DNA walkers[14,16,17,64] rely on hybridization with a DNA track and repositioning when the additional oligonucleotide components of these reactions are supplied externally. The need in this supply and the size of the motor, no smaller than 15-20 nucleotides required for a reliable specific hybridization and typically no larger than 50 nm, a persistence length of a double stranded DNA, are the limitations of these motors.

Our synthetic motors are protein-based. Potential advantages of proteins in the motor context include:

- The variety of protein-protein, protein-DNA and protein-small molecule interactions can be utilized.

- These interactions can be autonomous or externally controllable, e.g. through a supply of ligands or allostery (binding of an enzyme protein may be controlled by binding of a regulatory effector molecule to another site).

- Supramolecular structures can be engineered, particularly due to emerging secondary structure predictions[65] by AI.

Of our motors, Lawnmower is a burnt-bridges Brownian motor (as defined in 3.1) built on a bead that is functionalized with many protease molecules. Another motor, Tumbleweed, is a single molecule protein designed to step along a DNA track in presence of specific ligands.

3.3 Lawnmower

Lawnmower, introduced as a concept in Ref. [31], has many protease legs that bind and cleave a peptide 'lawn', biasing the diffusion of the motor hub as the legs have a higher affinity for uncleaved peptides (**Figure 7**A).

The first LM design[31] was based on a 16 nm quantum dot. Sulfo-SMCC was chosen as a linker between the quantum dots and proteases. With a length of 8.3 Å, it has an NHS group on one end (bound to an amine on the quantum dot) and maleimide on the other (bounds to the protease). To bind to the maleimide, a protease must feature a sulfhydryl, and several proteases were tested in that study after thiol reduction by TCEP (tris[2-carboxyethyl] phosphine) and primary amine thiolation with Traut's reagent (2-iminothiolane). Thiolated trypsin showed the best activity in cleaving fluorogenic peptides compared to other candidate proteases, including elastase, thrombin and pepsin.[31]

The new Lawnmower, studied here in Papers I and II, is instead built on a microsphere (M-270 amine Dynabeads with a 2.8 µM diameter, Thermo Fisher) but uses the same sulfo-SMCC linker and trypsin (**Figure 7**A). This larger hub increases polyvalency by five orders of magnitude compared to the quantum dot that accommodated only about 8 trypsin 'blades'[31] Polyvalency of the LMs was estimated by the rate of cleavage of fluorogenic peptides in bulk, as described in Paper II. Furthermore, the massive bead hub allows to confine and guide LMs within microchannels (**Figure 7**B), also making them more resistant to background solution perturbations.

The goal of our experiments was to achieve the Lawnmower motion in microchannels, which is interesting for network exploration applications such as biocomputation. To indicate motor activity, the motion has to be superdiffusive, that is, the motor displacement grows faster than linearly over time; the ways to calculate this are described in 3.4).

Moreover, the channels with a width proportional to the span on the motor (maximum distance between any two legs when they are bound to the substrate) has been modelled[33] to facilitate superdiffusive behaviour and directionality of the motion. Indeed, such a track makes a quasi-1D channel where the asymmetry between cleaved and fresh substrate creates a unidirectional bias. From simple geometrical calculations for a channel of the depth h, the minimum width when the bead can reach the channel floor is $w = 2\sqrt{h(2r - h)}$, where r – bead radius. For our channels, $h = 0.5$ µm, $w = 2.2$ µm.

We made the channels and functionalised them to get peptide lawn only on the channel floors. Details of fabrication (done not by the thesis author) and functionalization (done by the author) are described in Papers I and II. In short, a SiO$_2$ substrate was spin-coated with the resist CSAR 62, and the channels were patterned using electron beam lithography followed by dissolving the exposed resist so that the channels floors is bare SiO$_2$. It was then treated with oxygen plasma, followed by trimethylchlorosilane (TMCS) that made the channel bottom hydrophobic[36] which is necessary for the subsequent functionalization with peptides.

The lawn was built by attaching peptides to a brush of Pluronic F127. In addition to peptide attachment, functionalization with F127 passivates the surface against unspecific binding of trypsin, peptides and microspheres.[66] F127 is a non-ionic copolymer surfactant of PEG-PPG-PEG structure where PPG (polypropylene glycol) is hydrophobic and PEG (polyethylene glycol) is hydrophilic. F127s was thus attached through PPG to the hydrophobic SiO2 at the bottom of the channels, while the PEG with NHS modification was bound to the central lysine of the peptide. The channel walls made of resist therefore did not allow for functionalization and had no peptides, which was verified by imaging as the peptides were fluorogenic (**Figure 7**C).
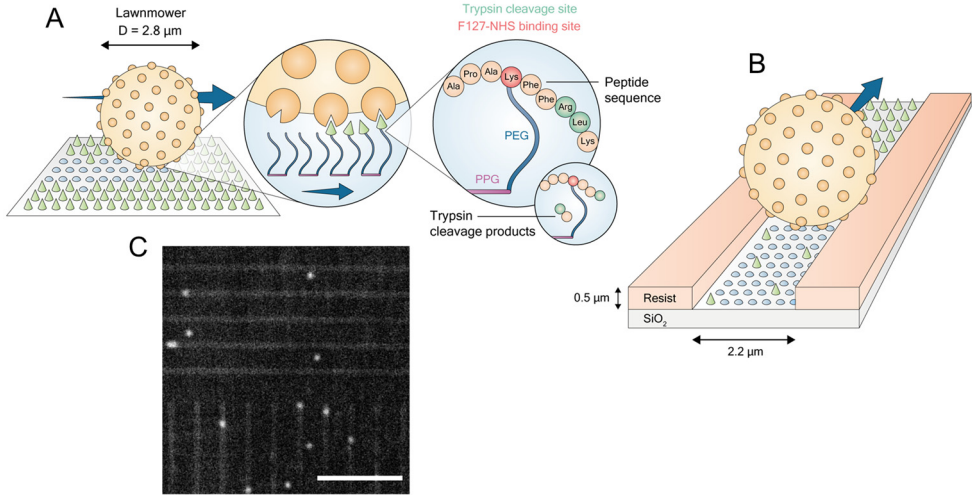
Figure 7. Lawnmower built on a microsphere. (A) Trypsin on the bead (yellow blades) are cleaving the peptides (green cones) attached to the F127 polymer brush. (B) Channels were fabricated to facilitate superdiffusive behaviour. (C) Functionalisation of channels with peptide lawn was verified by the signal of fluorogenic peptides cleaved by LMs and, for stronger signal, by externally added trypsin at 500 µg/ml. Brighter spots are due to LM autofluorescence. Scale bar: 50 µM. Adapted from the Paper II.

In the channels, we saw the motor activity indicated by the analysis of the motion as outlined below in 3.4, and in Papers I-II. The results from the Papers are summarized in 6.1 and 6.2.

3.4 How to characterize a particle-based molecular motor?

For a microsized motor such as LM, optical microscopy allows for tracking in solution with a high temporal resolution. However, the motor activity must be distinguished from diffusion if the motor does not show individual steps. Anomalous diffusion exponent can be one metric. For that, one needs to calculate mean square displacement. Firstly, square displacement is given by

$$\Delta r_j^2(t,\tau) \equiv \left[x_j(t+\tau) - x_j(t)\right]^2 + \left[y_j(t+\tau) - y_j(t)\right]^2 \quad (2)$$

where x_j and y_j are coordinates of the jth trajectory, t is time, and τ is the time lag of the measured displacement. If one is interested in diffusivity of an ensemble of N particles, the ensemble-averaged (EA) MSD is calculated:

$$\text{MSD}_{\text{EA}}(\tau) \equiv \left\langle \Delta r^2(0,\tau) \right\rangle = \frac{1}{N}\sum_{j=1}^{N} \Delta r_j^2(0,\tau). \quad (2)$$

For individual particles, trajectory-averaged (TA) MSD is calculated:

$$MSD_{TA}(\tau) = \overline{\Delta r_j^2(\tau)} = \frac{1}{T-\tau}\sum_{t=0}^{T-\tau}\Delta r_j^2(t,\tau) \quad (4)$$

where τ is time lag (e.g. interval between position recordings), T_j is the total duration of the jth trajectory[67].

Resulting from (3) or (4), MSD is time-dependent:

$$MSD = D_g t^\alpha. \quad (5)$$

Here, D_g is the generalized diffusion coefficient. Its units are length^2/time$^\alpha$, where t is time and α is the (anomalous) diffusion exponent. The system is driven by conventional diffusion when $\alpha = 1$. If the particles are less motile, then $0 < \alpha < 1$, and the system is subdiffusive. If $1 < \alpha < 2$, this is a superdiffusive behaviour that can be because the system is biased to a certain direction and/or exhibits bursts of larger displacements (jumps). Superdiffusive motion typically expected from artificial molecular motors and achieved by some LMs (**Figure 8**) in our ensembles.
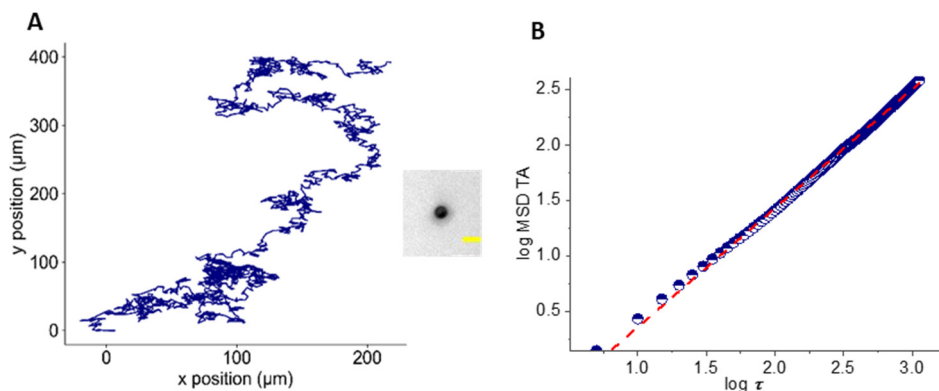
Figure 8. (A) Trajectory of a LM motor (inset, scale bar is 5 µm) on a 2D peptide lawn, total duration T of the trajectory is 11 265 s; (B) MSD$_{TA}$ as a function of log τ, where the time lag τ is less than 0.1T for substantial statistics. A linear fit (red dashed line) yields an anomalous diffusion exponent $\alpha = 1.1$, indicating superdiffusive motion. Adapted from the Paper I. Copyright 2022 American Chemical Society.

However, LMs and some other enzymatic motors[68] have saltatory dynamics, that is, bursts of superdiffusive motion are often intermediated by periods of low (subdiffusive) motility; for the results confirming this, please see 6.1−6.2, and Papers I−II. The low-motility periods undermine the accuracy of MSD$_{TA}$ analysis.

A metric we used to distinguish the larger displacements resulting from the periods of superdiffusive motion is kurtosis, the fourth standardized moment for the distribution of displacements Δr:

$$\kappa = \frac{\sum_{i=1}^{n}(\Delta r_i - \overline{\Delta r_i})^4}{n\sigma^4} \quad (6)$$

where n is the number of displacements in the distribution, σ is the standard deviation of the distribution. Kurtosis shows heaviness of tails in the displacement distribution compared to a normal distribution typical for regular diffusion of the particles. For LMs, this is shown in **Figure 21**B in 6.3. For a normal distribution, $\kappa = 3$. Higher κ means increasing probability of larger displacements, which is expected from a motor that exhibits superdiffusive bursts.[*]

3.5 Tumbleweed

While Lawnmowers have many legs exposed on a larger hub (microsphere or quantum dot), Tumbleweed is a single-molecule motor. It is assembled of three repressor proteins that bind to a DNA track.

The TW design was coined in Refs. [29,37], and consists of a methionine repressor MetJ, tryptophane repressor TrpR, and Diphtheria toxin repressor DtxR; these are assembled with coiled-coils (**Figure 9**). The repressors bind to specific DNA sequences in presence of respective ligands: *S*-Adenosyl methionine, trypthophane and Ni^{2+}. The pI of the construct is 5.8.
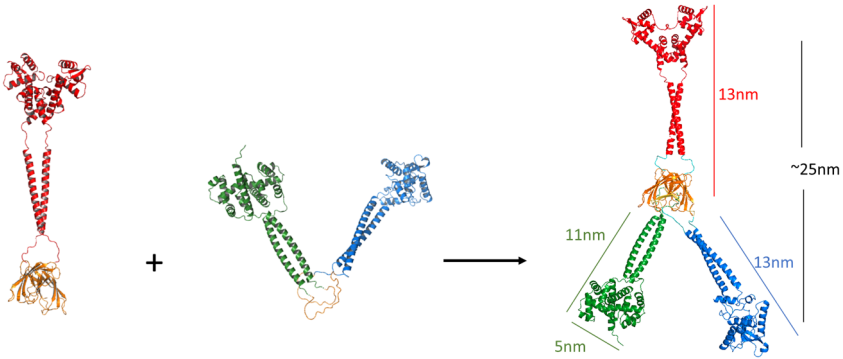
Figure 9. Tumbleweed is a dimer of TrpR, DtxR and MetJ repressors are depicted in green, red and blue respectively. The structure is predicted using AlphaFold.

The motor is designed to bind to corresponding sequences on a DNA track in presence of the above ligands, and step by changing one of the bound legs upon a

---

[*]You have read (or just came across) halfway through the thesis! This means there might be a prize waiting for you at Solid State Physics. See the location here: t.ly/v5COE, or ask me.

change of the ligands in a surrounding buffer. Specific binding of TW to the corresponding DNA sequences has been found in the surface plasmon resonance (SPR) experiments (carried out not by the author, data not published). However, the SPR experiments are technically limited to one change of the buffer and can show only binding and detachment of the motor but not stepping. Therefore, we designed fluorescence microscopy experiments.

We attempted observing TWs, labelled on their hub, using tracks attached to a micron sized bead, so that the fluorescence from multiple motors forms a circular pattern around the bead (**Figure 10**A). The radius of this circle (**Figure 10**) can be localized with a subdiffraction accuracy (< 10 nm), similarly to how it is done in cell surface optical profilometry [69]. However, detection of single steps of the motors was ultimately not successful due to unspecific binding of TWs to the beads and surrounding substrate.

The first idea for seeing the TW steps, developed in collaboration with the Jönsson group in Lund, was inspired by cell surface profilometry [69]. We attached tracks with three binding sites to streptavidin-modified beads (diameter 5 μm, Bangs Laboratories) and added labelled TWs, expecting their fluorescence to shape a circle around the bead. Its radius can be measured with subdiffraction precision. Once the TWs take a step, the radii of these circles were expected to narrow by 10-15 nm. However, the resolution was not sufficient, presumably due to non-specific binding of TWs to the beads.
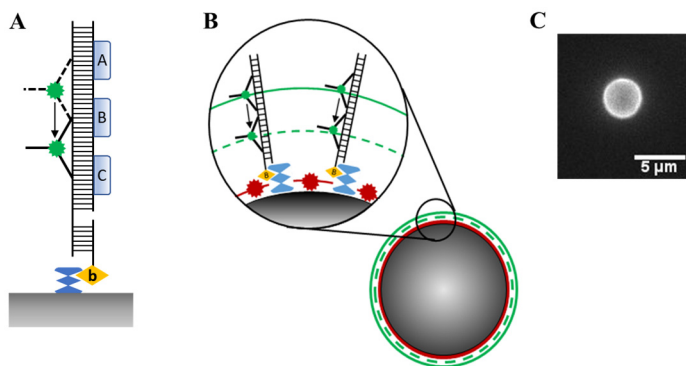
Figure 10. Optical profilometry of TWs on beads. (A) DNA tracks are immobilized on the beads via streptavidin-biotin linkage, and TW labelled on its hub is loaded on the track. (B) Multiple TWs in identical positions yield a circle of fluorescence (green), coaxial with reference red fluorophores on the bead. (C) Fluorescence of TWs on a bead.

To combat the non-specific binding, we tested several passivation approaches on passivate glass surfaces. The first is supported lipid bilayers (SLBs) made with 0.1 wt% of POPC and PE lipids. To POPC SLBs, DNA was attached via a cholesteryl

end modification, while the PE ones had biotin modification (2 mol% of biotinylated lipids) for attachment of biotinylated DNA.

Secondly, we tested two polymer brushes, PLL-g-PEG (PEG side chain 2 kDa) with 0.02% biotinylated PLL-g-PEG (PEG side chain 3.4 kDa) and F127. F127 (also used in LM experiments as described in 3.3) was assembled on glass treated to be hydrophobic as described in Ref. [66], also in presence of 5% Tween-20. Tween-20 is a non-ionic detergent often used to reduce non-specific binding to glass based on hydrophobic interaction. PLL-g-PEG yielded the best passivation of these (see **Figure 11** for its comparison to SLBs, and **Figure 12** for comparison with F127).
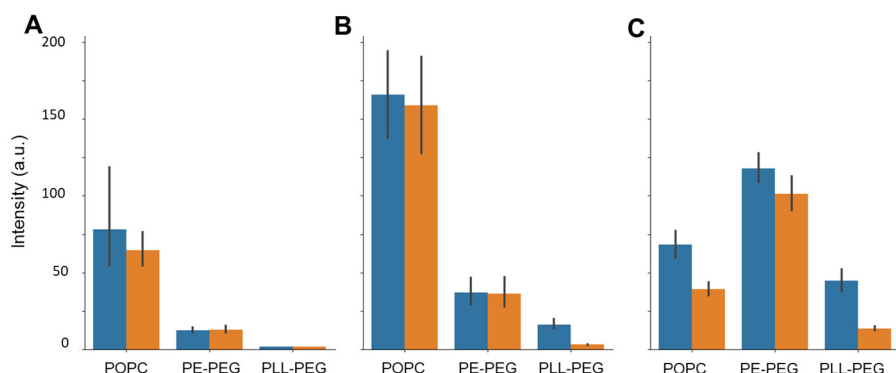
Figure 11. Passivation of glass against unspecific binding of TW. The passivation is expected to minimize non-specific binding in (A) absence of ligands and DNA, (B) absence of ligands and presence of DNA. In (A, B), blue and orange bars show intensities before and after an additional wash with the same buffer. When DNA and ligands are initially present (C), passivation is expected cause the highest loss of bound TW upon buffer switching from ligand-containing to no-ligand buffer. TW concentration is at 250 nM.
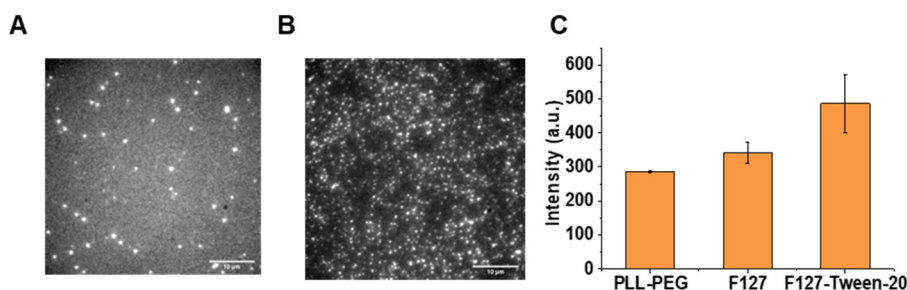
Figure 12. Non-specific binding of fluorescently labelled TW to glass passivated with (A) PLL-g-PEG and (B) Pluronic F-127. Scale bars are 10 µm, and the image contrast is adjusted for visibility. The number of fluorescent spots is clearly less in (A). (C) Mean intensities of TW unspecifically adsorbed to glass in presence of ligands but without DNA. PLL-g-PEG demonstrates superior passivation also by the intensity.

As another approach to see individual steps of TW, we designed a FRET assay (**Figure 13**) where TW is labelled with a donor (AlexaFlour 488-maleimide, reacted to thiol groups (cysteines) in the protein) on the TrpR foot, and DNA bears an acceptor (ATTO565) on corresponding site of the DNA track. In this configuration, FRET is not happening after TW takes a step but is re-established when it steps back. We are also attempting to see 3 colour FRET when another acceptor (AlexaFlour 647) is on the track along the direction of TW stepping; that way, stepping disrupts one FRET pair and makes another.
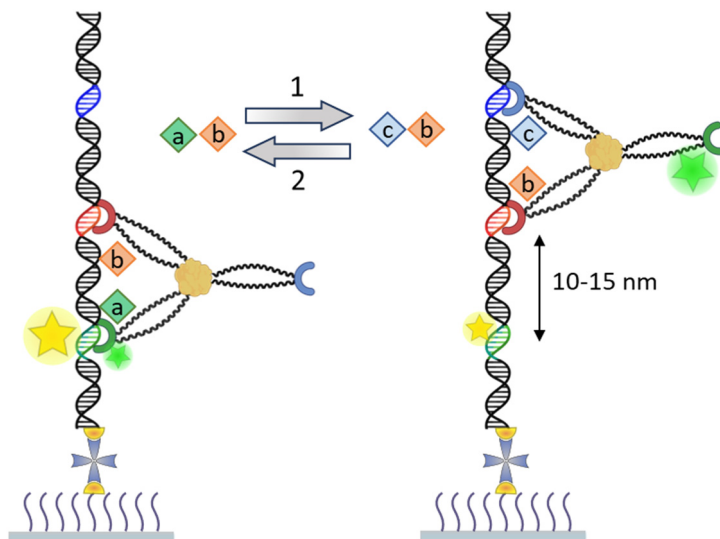
Figure 13. FRET experiment for the TW. TrpR foot (green) bears a donor (green star), while an acceptor (yellow star) is on the corresponding site of the DNA track. Once the motor has stepped at the first change of ligands (a, b) → (b, c), FRET disappears until the backwards step at the second change of ligands. The track is attached to a streptavidin (cross) on a biotinylated polymer brush on glass.

For future experiments, we additionally developed a DNA origami nanotube with TW binding sites. While dsDNA is considered approximately straight only on its persistence length of about 50 nm, the nanotube is more rigid and can be used in super-resolution or sub-diffraction localization (FIONA approach[60,61]) experiments where a TW makes multiple steps along the nanotube positioned laterally on glass. Our nanotube, based on the design by Bui et al.[70], is a six-helix bundle made by folding a single-stranded M13mp18 DNA with 170 staple oligonucleotides. These include the protrusion staples that form TW sites with 14 nm periodicity along the tube when bound to complementary oligos. The scheme of FRET experiment on such a nanotube is shown in **Figure 14**.

Figure 14. DNA nanotubes. (A) Scheme of a FRET experiment where binding sites (red, green, blue) for TW are built on staples of the nanotube. Green star – FRET donor, yellow star – FRET acceptor. (B) AFM image on mica, deposited in presence of 8 mM $MgCl_2$.
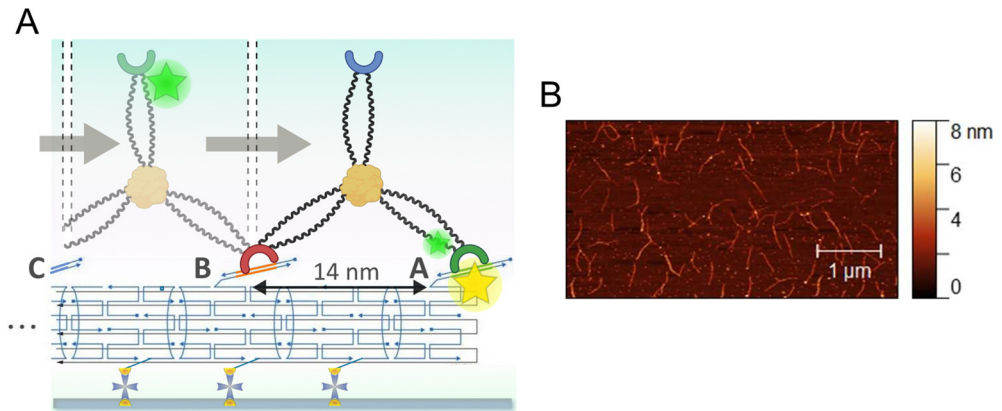
4 Fluorescence enhancement by semiconductor nanowires

4.1 Growth and properties of semiconductor nanowires

Nanowires (NWs) are structures with a high aspect ratio (here, we used the diameters ranging from 60 to 200 nm, with the length on μm-scale) which provide a large interface for surface functionalization. We grew gallium phosphide (GaP) III-V nanowires, that is, they consist of elements from the groups III (Ga) and V (P) of the Periodic table. The MOVPE (Metalorganic Vapor-Phase Epitaxy) GaP growth is based on the reaction of precursors (trimethylgallium and phosphine) at elevated temperature (pyrolysis):

$$Ga(CH_3)_3 + PH_3 \rightarrow GaP + 3CH_4$$
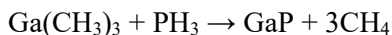
In this work, the growth was done (by the author) on a GaP(111)B wafer, that is, a substrate with the (111) crystal orientation, in an Aixtron 200/4 MOVPE reactor. To catalyse the growth, gold nanoparticles were deposited on the wafer. This was done (not by the author) either from aerosol using spark discharge[71], which yielded randomly positioned particles (and hence NWs, as used in Paper III), or by displacement Talbot lithography which results in periodic arrays (used in Paper IV). Prior to the growth, the substrate was annealed at 650°C to remove an inherent oxide layer and impurities.

The incoming precursors form a eutectic system with the nanoparticles, that is, a system where the melting temperature of Au is lower compared to pure material. Au melting is followed by the vapor-liquid-solid (VLS) growth (**Figure 15**): the vapor at 480°C causes supersaturation of the droplet, upon which solid GaP crystalizes under the droplet. This results in vertical (axial) growth of NWs. The diameter of a NW is then close to the diameter of the Au droplet. To widen the NWs, the temperature is increased to 600°C, and the phosphine flow is increased. This makes GaP preferentially crystallise on the sides of the NWs, enabling lateral (radial) growth.
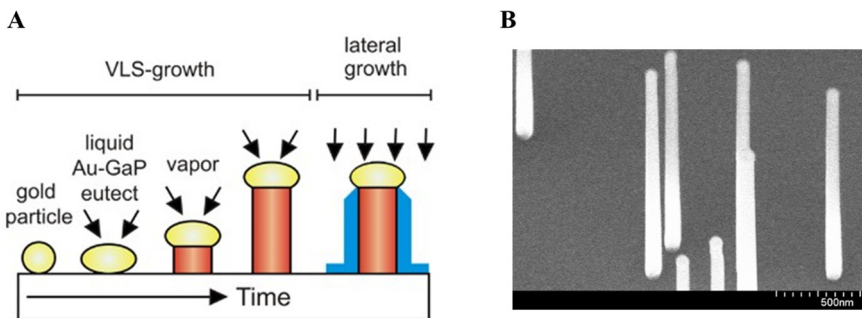
Figure 15. Nanowire growth by MOVPE. (A) Steps of the growth. In our system, axial growth was carried out at 480°C, and lateral (radial) – at 600°C. Adapted with permission from Ref. [72]. (B) SEM image of NWs under 30° tilt from the top view.

For the resulting NWs, diameter and length were measured using SEM. After that, they were coated with an oxide layer (Al_2O_3 in Paper III and SiO_2 in Paper IV) using atomic layer deposition (ALD). ALD allows for precise thickness of the layer; for the scheme of Al_2O_3 ALD, see **Figure 16**.
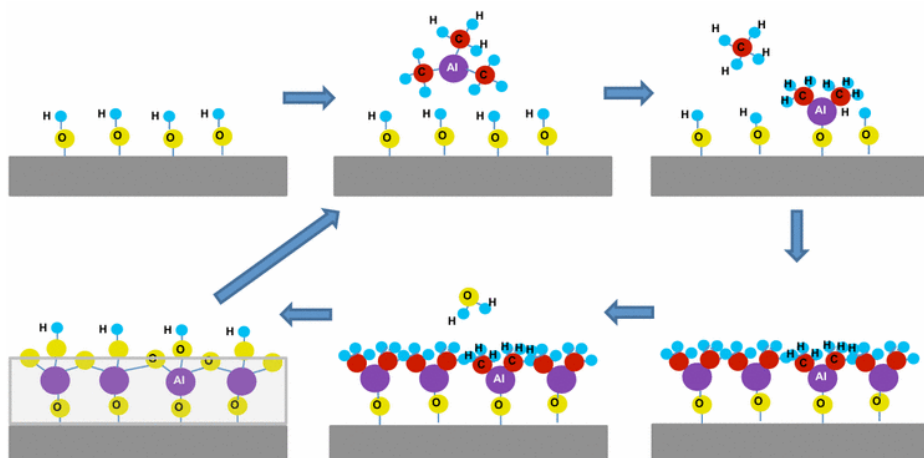
Figure 16. Atomic layer deposition (ALD) for Al_2O_3. Upper row, left to right, gaseous trimethylaluminum precursor is supplied and reacts with surface hydroxides. Then an inert gas purge follows, and water is introduced to form a new hydroxide layer. The pulses are thus looped. Reproduced from Ref. [73] under Creative Commons license. Copyright 2015 Springer Nature.

4.2 Surface functionalization of nanowires

In this thesis, we used biotinylated BSA to functionalize the NWs (**Figure 17**). BSA has a pI 5.1 and exhibits both positively and negatively charged groups which allow for adsorption on substrates with a different surface charge. It is widely available in the biotinylated formulation that can form the biotin-streptavidin noncovalent bond that is very stable.[74]

We loaded BSA in a PBS buffer with pH 7.0−7.2. It adsorbed from solution onto the oxide (Al_2O_3 or SiO_2) coating of the NWs. Isoelectric point of Al_2O_3 is at pH 9.0 as measured in Ref.[75], hence it is positively charged upon loading of BSA, while SiO_2, has the isoelectric point at pH 4.2 and a negative surface charge at these conditions. It was shown[75] that a larger amount of BSA is adsorbed onto Al_2O_3, although SiO_2 adsorbs it as well. This process takes only 5−15 minutes. We then remove unbound BSA, washing the platform with the buffer.
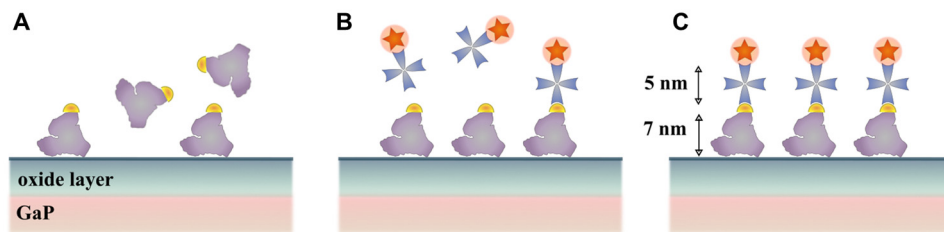
Figure 17. Functionalization of nanowire interface with BSA and fluorophores onto the oxide layer coating NWs. (A) Biotinylated BSA is adsorbed. (B) Excess BSA is removed, and streptavidin-conjugated fluorophores are added. (C) After another washing, only immobilized fluorophores stay. Small size of the system allows for lightguiding and enhancement of fluorescence by the NW.

For attachment of DNA to the NWs in Paper IV, we used the same surface chemistry, but with non-fluorescent streptavidin, which further binds to biotinylated DNA.

4.3 Why do nanowires enhance fluorescence?

The enhancement and guiding of fluorescence for proximal fluorophores has been demonstrated for NWs made of a range of semiconductor materials: ZnO [48,76,77], GaP[40,78], Si[42,43], InAs[44], GaAs[44,46]. It has been used for many optical biosensors.

Fluorescence enhancement is believed to stem from (i) lightguiding when fluorescence is coupled into the waveguiding modes of a NWs and then emitted directionally from the NWs [79–81]; (ii) enhancement of excitation; (iii) Purcell

enhancement of radiative emission rate; our studies of the effects (ii) and (iii) are reviewed in detail in 4.4 and 4.5. To describe the first effect, lightguiding, a NW is considered as an optical fiber with a diameter d, refractive index n_f, surrounded by a cladding or media with a refractive index n_{cl}. The number of waveguide modes depends on normalized optical frequency:

$$V = \pi \frac{d}{\lambda} \sqrt{n_f^2 - n_{cl}^2} \quad (7)$$

where d – diameter of the wire, λ – wavelength; this equation is derived from the Maxwell equations.[82] The fiber is single-mode when V is less than 2.405. In a single-mode fiber, most of the guided power is coupled into the fundamental mode HE_{11}. For the guiding of emission in this work, the NWs are thus single-mode for d less than 160−180 nm. As it has been shown for GaP NWs, the in-coupled power increases until $V \approx 1.75$ ($d \approx 120$ nm) and has peaks and dips upon the further increase in the diameter and hence in V.[51] Thus, most of the NWs used in this work are expected to show single-mode lightguiding.

4.4 Enhancement of excitation

Due to optical resonances, the GaP NWs are expected to cause field enhancement relative to the planar substrate, $M_{\mathrm{NW}}/M_{\mathrm{Planar}}$, where

$$M_{NW} = \frac{\int_{z=t_{oxide}}^{z=t_{oxide}+L} \int_{r=d/2+t_{oxide}}^{r=d/2+t_{oxide}+\Delta_{Fluor}} |E_{NW}(r,z)|^2 r\,dr\,dz}{L[(d/2+t_{oxide}+\Delta_{Fluor})^2 - (d/2+t_{oxide})^2]/2} \quad (8)$$

$$M_{\mathrm{Planar}} = \frac{\int_{z=t_{\mathrm{oxide}}}^{z=t_{\mathrm{oxide}}+\Delta_{\mathrm{Fluor}}} |E_{\mathrm{planar}}(z)|^2 dz}{\Delta_{\mathrm{Fluor}}} \quad (9)$$

Here, d and L – diameter and length of the wire, t_{oxide} – thickness of an oxide layer on the NW, Δ_{Fluor} – additional distance between the oxide layer and a fluorophore.

Excitation defines photobleaching rate of fluorophores until saturation is reached, after which the photobleaching is limited by emission rate. This proportionality allows us to use photobleaching rate as a metric for excitation enhancement in proximity of the NWs. We calculated photobleaching rate R from

$$I(t) \propto e^{-Rt}, \quad (10)$$

where t is the time and I is the fluorescence intensity on the NWs measured in an image.
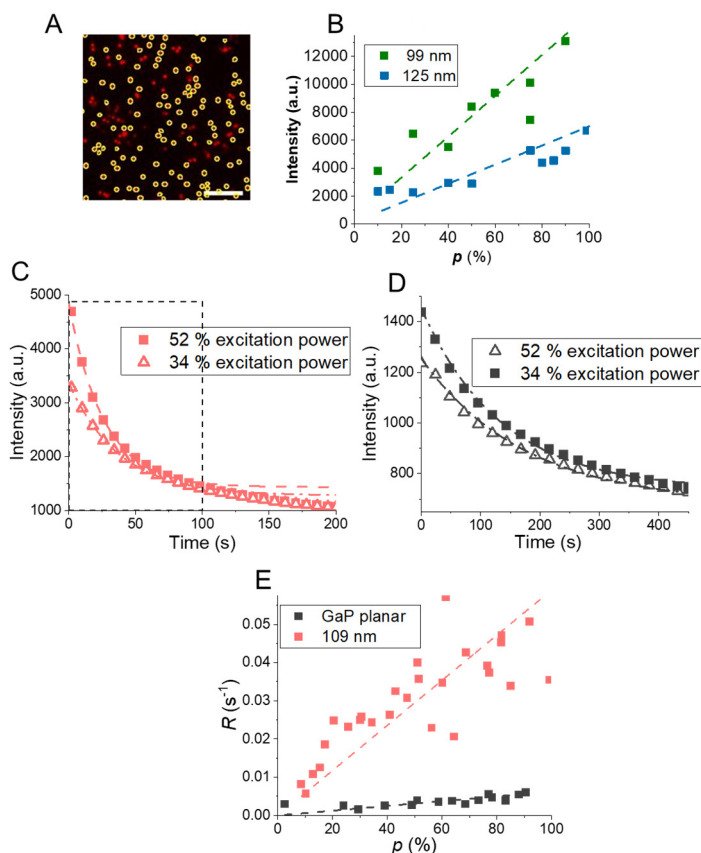
Figure 18. (A) Fluorescence (red dots) on GaP NWs, the yellow-encircled individual NWs were taken for the analysis; (B) Intensity on the NWs (diameters of 99 and 125 nm) grows linearly with the excitation power p; Photobleaching curves were recorded at varied power for the NWs (example spectra for the sample with d = 109 nm in C) and for planar GaP (D). Resulting photobleaching rates (E) also grow linearly with the power but are higher on NWs. Adapted from the Paper III with permission. Copyright 2023 Royal Society of Chemistry.

In Paper III, we model this enhancement and probe it experimentally, studying how it depends on NWs dimensions, distance from the NW interface, excitation wavelength and numerical aperture of the objective. The experiments were done using a widely used red dye Alexa Fluor 647 (Thermo Fisher Scientific), a streptavidin conjugate of which was attached to Al_2O_3 coating on the GaP NWs. The coating was made using atomic layer deposition (ALD) and functionalized with biotinylated BSA. The results of the Paper III are further summarized in 6.3.

4.5 Enhancement of emission

Furthermore, we estimated the emission modification by lifetime measurements. The radiative emission rate k_r on NWs is modified[79] by a Purcell factor C_p:

$$k_{r\,\text{NW}} = C_p k_{r\,\text{planar}} \quad (11)$$

In turn, fluorescence lifetime is given by

$$\tau = \frac{1}{k_r + k_{nr}} \quad (12)$$

where k_{nr} is a non-radiative emission rate. As k_{nr} is expected to be similar for fluorophores on NW and on planar substrate, the modification (11) of k_r can be calculated by measuring the lifetime.

For lifetime measurements, a microscope was equipped with a photodetector, which allowed for time-resolved measurement of emission in a NW-surrounding area of a diameter less than 1 μm. Decay curves were recorded at 2.5 MHz with a 256 ps binning resolution. We fitted these taking into account the instrument response function (IRF, shows distortion introduced to a decay curve by a delay in the instrument response). We expected that both the NWs and surrounding planar substrate will contribute to the output, therefore we applied a biexponential fit.

However, no significant difference was found between fluorophores on NWs and on the planar substrate (Table 1). However, we observed that the deviation between different NWs on the same platform is significant (see uncertainties in the first row of Table 1). Furthermore, the difference between the lifetimes can be not drastic because of a relatively low quantum yield of the used fluorophores. Indeed, if a quantum yield, defined as

$$\Phi = \frac{k_r}{k_r + k_{nr}} = \frac{\text{emission}}{\text{absorbance}} \quad (1)$$

is as low as 0.33 for the used fluorophores, the modification in k_r is relatively small.

	Exponent 1	Exponent 2
NWs $d = 66\pm3$ nm	0.4±0.2	1.22±0.15
Planar GaP	0.4±0.1	1.16±0.02

Table 1. Lifetimes of AlexaFluor 647 fluorophores on NWs and planar GaP substrate, coated with 10 nm Al2O3. Uncertainties are taken as standard deviation between NWs (row 1) or positions on the platform (row 2).

5 DNA-templated metal nanoclusters

5.1 Formation and fluorescence of DNA-templated nanoclusters

DNA bases can bind Ag ions, with a higher affinity[54] to cytosine and guanine than to adenine and thymine. Resulting DNA-templated silver nanoclusters (NCs) are fluorescent, with the spectra depending on the DNA sequence. Fluorescence is attributed to two phenomena: (i) ligand-to-metal charge transfer from electron-rich N atoms in DNA to the NCs; (ii) dipole-mediated coupling of the surface plasmon of Ag with the emitter, which causes the emission spectra of the NCs to be dependent on the excitation wavelength.[83]

Because of high affinity of Ag to guanine bases, fluorescence of a NC templated by a single-stranded DNA increases in nanometer-scale proximity of another, guanine (G)-rich, DNA strand. A library of NCs-templating and matching G-rich sequences was reported in Ref. [53], and recently expanded in Ref. [52] with the help of DNA sequencing. These NCs have been used in junction beacons[84] (of design similar to our beacon depicted in Figures 6 and 24) where the two strands are brought together by hybridisation with a target DNA. Such constructs have been used in biosensing for detection of DNA[84], and shown to detect single-nucleotide differences in the target sequence as that defines the relative positions of NC-templating and G-rich strands (**Figure 19**). A design based on a hairpin instead has also been used to detect miRNA.[85] These studies were performed in bulk and detection limit for the nucleic acids was in high pM to low nM range. By coupling with DNA aptamers, Ag NCs have also been used for detection of thrombin[86] and ATP[57].
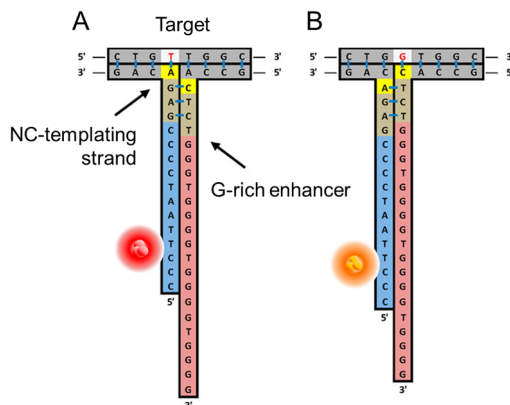
Figure 19. NC-based probes where the colour of fluorescence changes between red (a) and orange (B) upon a single-nucleotide replacement T→G in the target strand. Adapted with permission from Ref. [84] Copyright 2012 American Chemical Society.

Preparation of NCs in our study is described in detail in Paper IV. It involves a reducing agent, for which we used $NaBH_4$ in aqueous solution, added to the $AgNO_3$−DNA solution. All manipulations with the resulting complexes we did at room temperature, which is beneficial for a biosensor as opposed to heating often used[53,84] in this stage. For our beacons, samples after heating showed similar or even less fluorescence compared to prepared at room temperature.

The challenge is thus to increase the contrast between NCs activated by a small concentration of a target and nonactive weekly fluorescent NCs. In the Paper IV, we address this by employing the GaP NWs.

6 Summary of results

6.1 Paper I. Through the eyes of creators: observing artificial molecular motors

This paper is predominantly a review for the methods to observe and characterize artificial molecular motors. However, in addition to reviewing the existing literature, we for the first time present in Sections 3.1−4.1 of the Paper the Lawnmower based on a µm-sized bead, and the experiments where its motion is observed in quasi-1D peptide channels which are described in 3.3. The motion is analysed using MSD_{TA} (as described in 3.4) and average speed v over a trajectory (Figure 20). Anomalous diffusion exponents α are then calculated from MSD_{TA}.

We demonstrate that some LMs show superdiffusive motion on 2D and in channels, however subdiffusive low-motile behaviour is also manifested for many of them. By contrast, the diffusion exponents and speeds for non-motor unmodified particles show regular diffusion, clustering more tightly around mean values, $\alpha = 1$ and $v = 0.09$ µm/s.

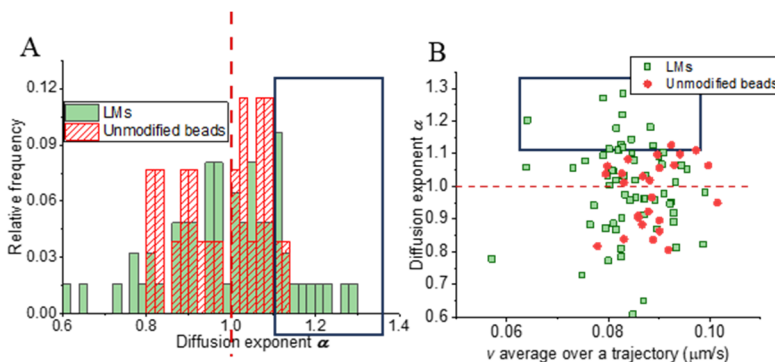**Figure 20**. Motion of Lawnmowers in 2.2 µm wide channels functionalized with peptides, and of unmodified beads (not motors) in bare channels. Speeds are sampled over 10 s intervals, then averaged over a trajectory. Superdiffusive LMs are enframed. Adapted from the Paper I with permission. Copyright 2022 American Chemical Society.

In summary, we found and average speed v indicates but not demonstrates the superdiffusive motion clearly, as this type of motion is intermitted with low-motile and diffusive behaviour. In Paper II, we suggest another analysis that is based on displacements.

6.2 Paper II. The Lawnmower: an autonomous, protein-based artificial molecular motor

In this manuscript, we analyse the behaviour of Lawnmowers in peptide-functionalized channels (described in 3.3) using their displacements (in addition to the MSD analysis) and kurtosis. This works also contains results for Lawnmowers on two-dimensional substrates. The author of this thesis performed some experiments on those to verify the functionalization of SiO_2 with the peptide lawn (**Figure 8**). However, the 2D experiments in this Paper were not performed by the author, hence we are not focusing on those here. In short, the LMs on 2D substrates showed saltatory dynamics where larger displacements were intermediated by periods of low motility. This behaviour is very similar to the dynamics in channels, and it lowers the anomalous diffusion exponent α despite it indicating superdiffusive behaviour. Therefore, we chose to analyse displacement distributions instead.

Here, we extracted all displacements (**Figure 21**), but for the LMs we excluded the parts of trajectories where they were visibly stuck, as these do not exhibit a motor activity. The displacement distribution (**Figure 21**B) for the LMs shows a kurtosis $\kappa > 3$, indicating the presence of larger displacements than for non-motor reference beads. This agrees with a model of directionally biased motion (model not by the author of the thesis), also suggested in the Paper. In summary, this strengthens the evidence of the LM motor activity.

The analysis approach presented in this Paper can in future be used to study the LMs in channels of a varied width, as the width is expected to affect processivity of the motion and the extent of superdiffusive behaviour[33]. It could also be interesting to experiment with curved channels. These ideas are described in the Outlook.
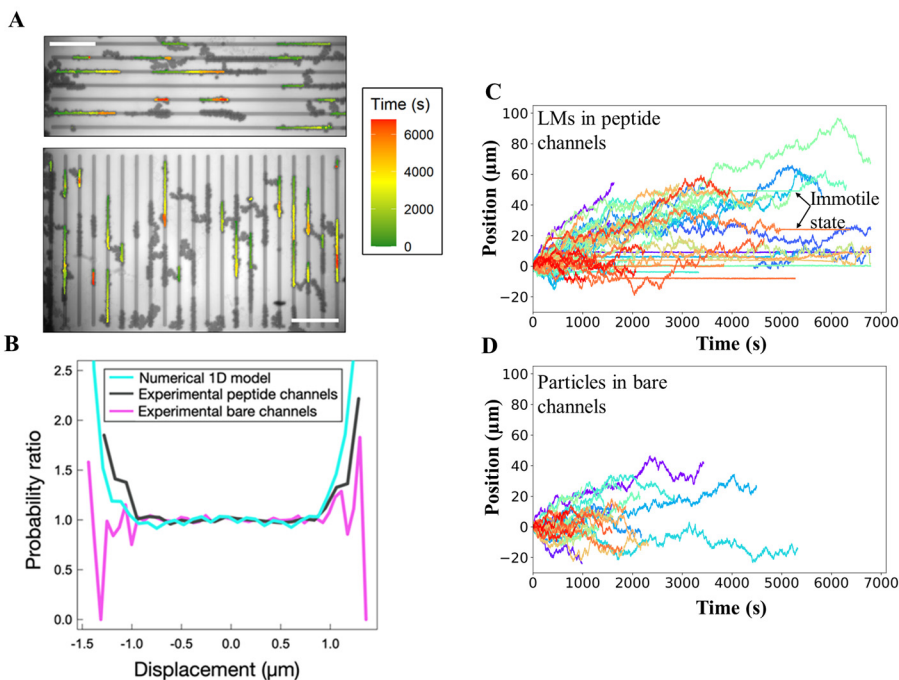
Figure 21. (A) Overlay of all Lawnmower positions (dark spots) in the microchannels. Of those, we analysed the trajectories (colored from green to red to illustrate the duration) that did not contain collisions or jumps of the particles out of the channels. Scale bar is 50 μm. These trajectories yield the displacements (C) which we compared with the displacements (D) of non-motor beads in channels without the peptides. (B) Distribution of displacements compared with a model of superdiffusive motion. The experiment and the model show heavy tails for the distribution for LMs. Adapted from the Paper II.

In this paper, we additionally estimated polyvalency of the LMs which is an important characteristic of such motors. For that, we compared the rate at which a known amount of LMs cleave fluorogenic peptides in bulk buffer solution with the cleavage rate for different concentrations of trypsin (**Figure 22**). Calculating the concentration ratio, we obtained an average of $(5\pm1)\cdot10^5$ trypsins per LM, that is, 0.02 trypsins per nm^2 of the surface area. From this, given the thickness of the F127 brush and the size a trypsin molecule, one can estimate that $\sim2\cdot10^3$ trypsins are simultaneously cleaving the lawn. This illustrates polyvalency of the bead-based LMs; for comparison, the quantum dot-based LM of the first design[31] featured only 8 trypsins.
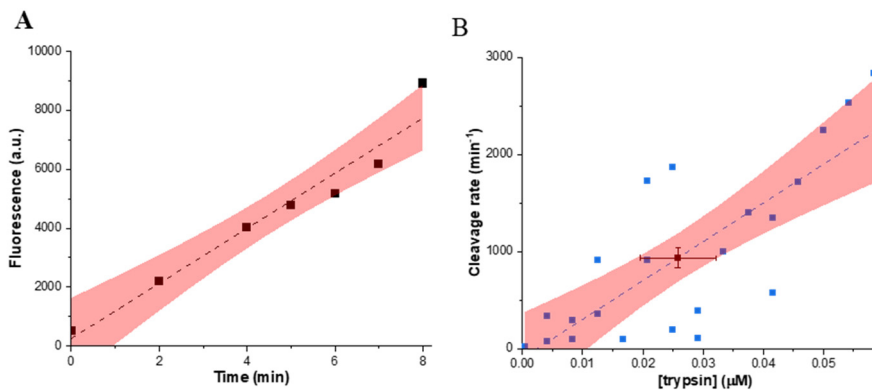
Figure 22. (A) Time-dependent cleavage of fluorogenic peptides for LMs at the concentration $3 \cdot 10^7$ mL^{-1}. (B) Cleavage rates of varied concentration of trypsin (blue dots) and the same concentration of peptides as in (A). The cleavage rate of LMs (dark red dot) is same as the cleavage rate of trypsin at $(2.6 \pm 0.6) \cdot 10^{-8}$ M within a 95% confidence band (pink). Reproduced from the Paper II.

6.3 Paper III. Fluorescence excitation enhancement by waveguiding nanowires

In this Paper, we study fluorescence excitation enhancement by GaP nanowires. As explained in 4.3, fluorescence enhancement is an interplay of three effects: the enhancement of excitation, the Purcell emission enhancement, and lightguiding. In previous experimental publications on local field enhancement, where ZnO [48] and GaAs[46,46] nanorods were studied, these three were estimated as a whole, by measurements of absolute intensity. This approach limits the results to the specific wavelengths used in those studies, and requires calibration of the measurements, as the intensity changes upon photobleaching.

We employ GaP that, unlike ZnO and GaAs, has negligible absorbance[87] in most of visible wavelengths. Besides that, we disentangle the enhancement of excitation from the other two effects. In this Paper, we study the excitation enhancement experimentally (done by the author) for a range of NW diameters 60-220 nm (Figure 23), and, by modelling (done not by the author), for other wavelengths and numerical apertures of the illumination objectives. For the experiment, we measure photobleaching rate; more details of this approach, not typical for a quantitative fluorescence study, are found in 4.4.
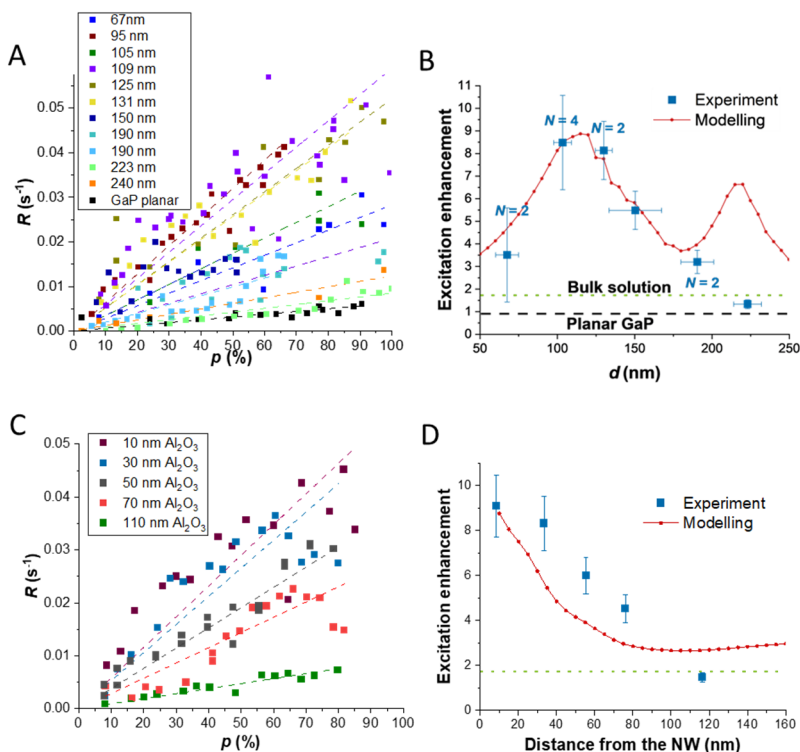
Figure 23. (A) Increasing with the excitation power, the photobleaching rates are highest for the diameters 90-130 nm, indicating (B) a peak in the excitation enhancement. The enhancement was calculated as described in 4.4. (C)–(D)The enhancement depends strongly on the fluorophore-to-NW distance controlled by the thickness of Al_2O_3 coating. Adapted with permission from the Paper III. Copyright 2023 Royal Society of Chemistry.

For this data, the NWs with a diameter 90-130 nm are optimal for excitation enhancement for red fluorophores (Figure 23B), and this does not noticeably depend on the vertical length of the NWs. For shorter excitation wavelengths, the peak is predicted to shift to smaller diameters in a manner that keeps a constant optical path around the circumference of the NW, proportional to $d\mathrm{Re}(n(\lambda))/\lambda$, where n is the refractive index at the wavelength λ. This enhancement decays within 100 nm form the NW (Figure 23D).

6.4 Paper IV. Biosensor for short DNA based on fluorescent silver nanoclusters and semiconductor nanowires

In this manuscript, we designed a nanocluster beacon (for review of the NC technology, see 5.1) that attaches to GaP NWs and is used to detect DNA in solution. The fluorescence-enhancing NWs thus increase the sensitivity of the biosensor through enhancing the intensity contrast between brightly and weekly fluorescent NCs in presence and absence of the target respectively.

For that, we adapted the DNA sequences recently shown to be optimal for templating NCs with red fluorescence[52] and added nucleotides that are complementary to a target 42-nucleotide DNA. Furthermore, we extended 5' end of the G-rich enhancer so that it is complementary to the biotinylated anchor that binds to streptavidin on the NWs. That way, only the beacons assembled in the presence of the target can bind to the NWs, while low-fluorescent NCs in absence of the target cannot attach. One challenge we encountered is the positioning of this anchoring sequence: activation of the NCs was not successful when it was on the 3' end of the G-rich enhancer, that is, close to the location of NCs in the assembled beacon. This indicates the importance of flexibility of the polyG sequences in the beacon.
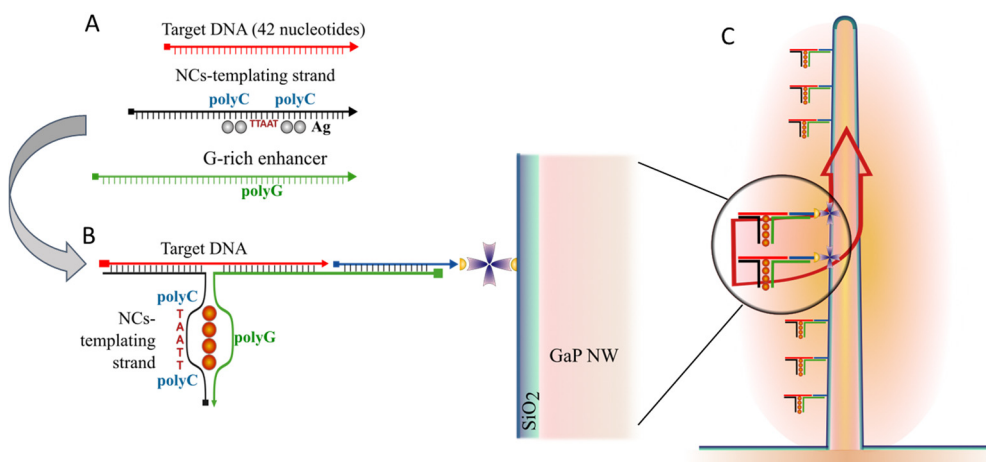
Figure 24. NC beacon on a NW. (A) Non-activated low-fluorescent NCs on the templating DNA are added to a solution that contains target and G-rich enhancer DNA. (B) The beacon binds to a NW. (C) The NW enhances and guides fluorescence of multiple beacons. Adapted from the Paper IV.

We used NW platforms with a high density of 1.2 μm^{-2} and a diameter of 118±5 nm; the NWs were coated with 10 nm of SiO$_2$. The beacons were assembled in bulk

and added to the flow chambers with NWs. We achieve detection of nanomolar concentrations of the targets, with a perspective to further improve the sensitivity.

Another challenge in this system is that the subsequent washing with the buffer, intended to remove all non-activated beacons (hence, not bound to the NWs) and increase the signal-to-noise ratio, resulted in a significant loss of signal and is therefore not beneficial for sensitivity. Although this step is not mandatory for our biosensor as the signal from non-activated NCs is negligible (blue dots in **Figure 25**), better immobilization could accumulate more NCs and help to lower the background signal after washing. This can be explored in future studies.
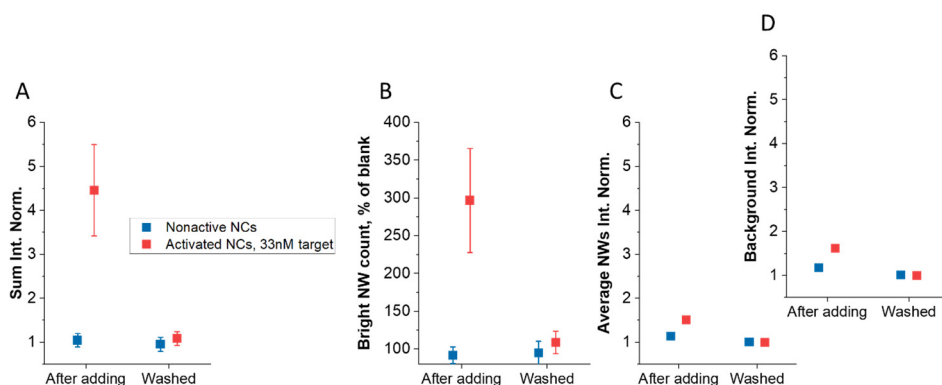

Figure 25. Fluorescence of activated and non-activated NCs normalized on a blank (same sample before adding the NCs). (A) Sum intensity on the NWs; (B) Number of bright NWs;(C) Average intensity on a NW; (D) Average intensity outside the lightguiding NW locations (background). From the Paper IV.

7 Outlook

Artificial nano- and microsystems that harness functional molecules are a major field of studies presently. The Nobel Prizes for click- and bioorthogonal chemistry in 2022, for synthetic molecular motors in 2016 and for super-resolution microscopy in 2014 are just a few indicators of this. Artificial molecular motors are currently tested as a part of even more complex constructs such as a synthetic cell[3]. Due to superdiffusive behaivoir, the motors are efficient for exploring complex networks, which is needed in biocomputing[35,36] or transportation of medical cargo in wound dressings[88] and possibly in implants. One can further imagine such motors to move on cellular membranes and along natural cytoskeletal or nucleic acid tracks in living cells.

In this thesis, we studied artificial molecular motors that were built for microscale (Lawnmower) and nanoscale (Tumbleweed) motion. Performance of Lawnmowers, characterized in Papers I-II, can potentially be improved by varying the density of peptide lawn, and, for channels, the dimensions. The span of LM 'blades' may also be altered by changing the linker between the bead and proteases. To further characterize the LMs, it is interesting to try channel geometries other than quasi-1D channels. Channels with turns will show the probability for the LMs to take change direction and could be useful for molecular motor-based biocomputing[35,89] and other applications that involve network exploring. In one experiment, we used square-shaped channel networks, and observed that LMs were able to take 90° turns (**Figure 26**), and their behavior was otherwise similar to that in the quasi-1D channels.

In our LM experiments, we saw a number of motors jumping out of the channels (**Figure 21**A). Such motion in a vertical plane can be used on a 3D substrate to measure the force generated by the particle-based motor. A single-molecule motor like Tumbleweed is not significantly affected by gravity, but a force measurement can be realized when a cargo of a known size and mass is attached to the motor. The generated force is a metric useful for comparison between motors.
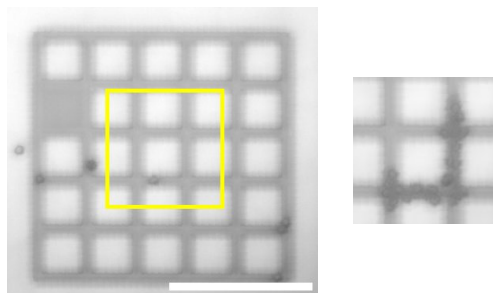
Figure 26. LMs in a square-shaped network of channels. Scale bar is 50 µm. Inset is the trajectory of the motor in the yellow frame, which includes 90° turns.

Observing the steps of Tumbleweed has been particularly challenging because of their sub-diffraction size and prominent nonspecific adsorption of the motors to the substrate. We found that the PLL-PEG surface chemistry is the best of the studied to passivate the substrate. To achieve sub-diffraction characterization of the nanosized steps of Tumbleweed, we tried the profilometry approach on the microbeads and further designed a FRET characterization study of its nanosized steps that will be continued in our laboratory. We also adapted DNA origami nanotubes to accommodate binding sites for the Tumbleweed, and the nanotubes can also be attached to the nanowires. Alternatively, they can be fixed on the glass to visualize the stepping using sub-diffraction localization (FIONA[60,61]) or super-resolution microscopy. Of super-resolution techniques, MINFLUX[90,91] provides a resolution of below 5 nm and is therefore promising.

Another potential way to detect the sub-diffraction movements is to use NWs. As shown in Paper III, NWs-induced fluorescence enhancement and lightguiding depends on the distance from the nanowire and decays within 100 nm from the nanowire. Lightguiding by the NWs is also a near-field effect. This was used to track labelled actin filaments using myosin-functionalized NWs: the fluorescence was coupled into NWs when the filaments climbed onto those.[40] For TW, dsDNA or origami tracks can be attached to NWs (**Figure 27**) to detect small movements of the motors stepping towards or from the NWs.

For a LM-type motor that is sufficiently small, e.g. a quantum dot-based LM[31], a fluorogenic peptide lawn can be assembled on the NWs. From there, one can think of guiding the motors along a row or array of NWs that are precisely positioned using Talbot lithography.
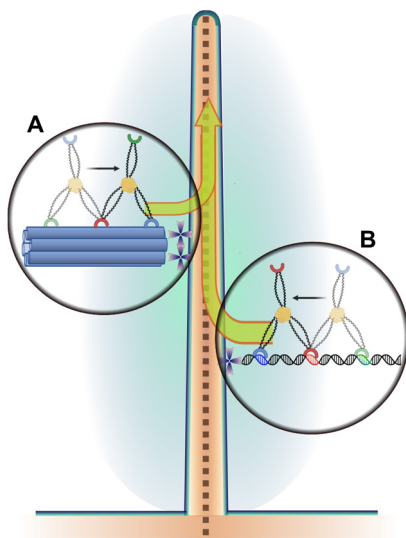
Figure 27. Within 50−100 nm from its surface, NWs can enhance and in-couple fluorescence of TWs walking towards the NW along an attached (A) DNA nanotube (depicted not to scale) or (B) double-stranded DNA.

In this thesis, we achieved a quantitative understanding of fluorescence enhancement in GaP NWs, which provides guidance as to what dimensions are optimal for a fluorophore of interest. As a next step, it can be interesting to test fluorophores with a high quantum yield, which could harness the Purcell emission enhancement better than those used in this thesis (see 4.5).

As the NWs have a high surface-to-volume ratio and their oxide coating is compatible with a variety of surface chemistries, self-assembly of fluorescence emitters on the NWs is interesting. In this thesis, we designed a molecular beacon that is based on DNA-templated fluorescent nanocluster and binds to the NWs when assembled in presence of the target DNA. Other DNA systems such as aptamers and hairpins can be explored for assembly on the NWs that would allow guiding and enhancement of fluorescence. These can be mounted on DNA nanotubes.

In this thesis, semiconductor NWs enhance the signal of fluorophores. Plasmonic-based detection can be a promising alternative. For this, plasmonic noble metal nanostructures, including DNA-templated metal nanoclusters, can be employed. For the clusters, plasmonic excitation is indicated, even though it is traditionally believed to be due to multiple transitions between the Kohn−Sham levels of single particle ground state orbitals, whereas for short atomic chains it is one transition.[92,93] While plasmonic properties of the clusters need further studies, such properties are well-documented for noble metal nanoparticles which can also be mounted onto semiconductor NWs.[94] Label-free biosensing for such systems will be enabled by

the fact that plasmonic resonance frequencies are sensitive to the dielectric constant of the surroundings. Alternatively, arrays of semiconductor nanowires coated with plasmonic nanostructures creating Raman hotspots have shown[95] to be a promising platform for surface-enhanced Raman scattering (SERS) biosensing.

For future applications, the MOVPE growth of NWs has the limitation of low throughput (each growth takes around an hour). A competitor is the aerotaxy method where catalyzed growth of NWs is done within minutes in the gas phase[96], although with somewhat less of control over their dimensions. For aerotaxy NWs, fluorescence enhancement has recently been demonstrated in our laboratory.[41]

It is challenging for optical NW biosensors to compete with well-established methods such as ELISA or qPCR; however, their performance may be improved by click-chemistry or other chemistries allowing for better specific binding and immobilization of molecules on their surface.

8 References

1. Bustamante, C., Chemla, Y. R., Forde, N. R. & Izhaky, D. Mechanical processes in biochemistry. *Annu Rev Biochem* **73**, 705–748 (2004).

2. Kopperger, E. *et al.* A self-assembled nanoscale robotic arm controlled by electric fields. *Science* **359**, 296–301 (2018).

3. Zhan, P., Jahnke, K., Liu, N. & Göpfrich, K. Functional DNA-based cytoskeletons for synthetic cells. *Nat. Chem.* **14**, 958–963 (2022).

4. Xin, L., Zhou, C., Duan, X. & Liu, N. A rotary plasmonic nanoclock. *Nat. Commun.* **10**, (2019).

5. Uhl, E., Mayer, P. & Dube, H. Active and Unidirectional Acceleration of Biaryl Rotation by a Molecular Motor. *Angew. Chem. - Int. Ed.* **59**, 5730–5737 (2020).

6. Grill, K. & Dube, H. Supramolecular relay-control of organocatalysis with a hemithioindigo-based molecular motor. *J. Am. Chem. Soc.* **142**, 19300–19307 (2020).

7. Romeo-Gella, F., Corral, I. & Faraji, S. Theoretical investigation of a novel xylene-based light-driven unidirectional molecular motor. *J. Chem. Phys.* **154**, 064111 (2021).

8. Gilissen, P. J. *et al.* Molecular motor-functionalized porphyrin macrocycles. *Nat. Commun.* **11**, (2020).

9. Stolz, S., Gröning, O., Prinz, J., Brune, H. & Widmer, R. Molecular motor crossing the frontier of classical to quantum tunneling motion. *Proc. Natl. Acad. Sci. U. S. A.* **117**, 14838–14842 (2020).

10. Ni, J. S. *et al.* A Photoinduced Nonadiabatic Decay-Guided Molecular Motor Triggers Effective Photothermal Conversion for Cancer Therapy. *Angew. Chem. - Int. Ed.* **59**, 11298–11302 (2020).

11. Shi, Z. T. *et al.* Visible-Light-Driven Rotation of Molecular Motors in Discrete Supramolecular Metallacycles. *J. Am. Chem. Soc.* **143**, 442–452 (2021).

12. Zhou, Q. *et al.* Unidirectional rotating molecular motors dynamically interact with adsorbed proteins to direct the fate of mesenchymal stem cells. *Sci. Adv.* **6**, (2020).

13. Roke, D., Wezenberg, S. J. & Feringa, B. L. Molecular rotary motors: Unidirectional motion around double bonds. *Proc. Natl. Acad. Sci. U. S. A.* **115**, 9423–9431 (2018).

14. Hu, X., Zhao, X., Loh, I. Y., Yan, J. & Wang, Z. Single-molecule mechanical study of an autonomous artificial translational molecular motor beyond bridge-burning design. *Nanoscale* **13**, 13195–13207 (2021).

15. Liu, B. *et al.* Design and mechanisms of antifouling materials for surface plasmon resonance sensors. *Acta Biomater* **40**, 100–118 (2016).

16. Tomov, T. E. *et al.* DNA Bipedal Motor Achieves a Large Number of Steps Due to Operation Using Microfluidics-Based Interface. *ACS Nano* **11**, 4002–4008 (2017).

17. Wickham, S. F. J. *et al.* Direct observation of stepwise movement of a synthetic molecular transporter. *Nat. Nanotechnol.* **6**, 166–169 (2011).

18. Bazrafshan, A. *et al.* Tunable DNA Origami Motors Translocate Ballistically Over µm Distances at nm/s Speeds. *Angew Chem.* **59**, 9514–9521 (2020).

19. Bazrafshan, A. *et al.* DNA Gold Nanoparticle Motors Demonstrate Processive Motion with Bursts of Speed Up to 50 nm Per Second. *ACS Nano* **15**, 8427–8438 (2021).

20. Yehl, K. *et al.* High-speed DNA-based rolling motors powered by RNase H. *Nat Nanotechnol* **11**, 184–190 (2015).

21. Blanchard, A. T. *et al.* Highly Polyvalent DNA Motors Generate 100+ pN of Force via Autochemophoresis. *Nano Lett.* **19**, 6977–6986 (2019).

22. Stepp, W. L., Merck, G., Mueller-Planitz, F. & Ökten, Z. Kinesin-2 motors adapt their stepping behavior for processive transport on axonemes and microtubules. *EMBO Rep.* e201744097 (2017) doi:10.15252/embr.201744097.

23. Friel, C. T. & Howard, J. Coupling of kinesin ATP turnover to translocation and microtubule regulation: One engine, many machines. *J. Muscle Res. Cell Motil.* **33**, 377–383 (2012).

24. Howard, J. *Mechanics of Motor Proteins and the Cytoskeleton*. (Sinauer Associates, Inc., 2001).

25. Pierobon, P. *et al.* Velocity, processivity, and individual steps of single myosin V molecules in live cells. *Biophys. J.* **96**, 4268–4275 (2009).

26. Srivastava, G. *et al.* Driving a Third Generation Molecular Motor with Electrons Across a Surface. *ACS Nano* **17**, 3931–3938 (2023).

27. Lund, K. *et al.* Molecular robots guided by prescriptive landscapes. *Nature* **465**, 206–210 (2010).

28. Korosec, C. S. *et al.* Substrate stiffness tunes the dynamics of polyvalent rolling motors. *Soft Matter* **17**, 1468–1479 (2020).

29. Small, L. S. R. *et al.* Construction of a Chassis for a Tripartite Protein-Based Molecular Motor. *ACS Synth. Biol.* **6**, 1096–1102 (2017).

30. Vecchiarelli, A. G., Hwang, L. C. & Mizuuchi, K. Cell-free study of F plasmid partition provides evidence for cargo transport by a diffusion-ratchet mechanism. *Proc Natl Acad Sci U A* **110**, 1390–1397 (2013).

31. Kovacic, S. *et al.* Design and construction of the lawnmower, an artificial burnt-bridges motor. *IEEE Trans. Nanobioscience* **14**, 305–312 (2015).

32. Blanchard, A. T. Burnt bridge ratchet motor force scales linearly with polyvalency: a computational study. *Soft Matter* **17**, 6056–6062 (2021).

33. Korosec, C. S., Zuckermann, M. J. & Forde, N. R. Dimensionality-dependent crossover in motility of polyvalent burnt-bridges ratchets. *Phys. Rev. E* **98**, (2018).

34. Lard, M. *et al.* Ultrafast molecular motor driven nanoseparation and biosensing. *Biosens. Bioelectron.* **48**, 145–152 (2013).

35. Salhotra, A. *et al.* Prolonged function and optimization of actomyosin motility for up scaled network-based biocomputation. *New J. Phys.* **23**, (2021).

36. Lindberg, F. W. *et al.* Controlled Surface Silanization for Actin-Myosin Based Nanodevices and Biocompatibility of New Polymer Resists. *Langmuir* **34**, 8777–8784 (2018).

37. Bromley, E. H. C. C. *et al.* The tumbleweed: Towards a synthetic protein motor. *HFSP J.* **3**, 204–212 (2009).

38. Dorfman, A., Kumar, N. & Hahm, J. I. Nanoscale ZnO-enhanced fluorescence detection of protein interactions. *Adv. Mater.* **18**, 2685–2690 (2006).

39. Dorfman, A., Kumar, N. & Hahm, J. I. Highly Sensitive Biomolecular Fluorescence Detection Using Nanoscale ZnO Platforms. *Langmuir* **22**, 4890–4895 (2006).

40. Ten Siethoff, L. *et al.* Molecular motor propelled filaments reveal light-guiding in nanowire arrays for enhanced biosensing. *Nano Lett.* **14**, 737–742 (2014).

41. Valderas-Gutiérrez, J. *et al.* Enhanced Optical Biosensing by Aerotaxy Ga(As)P Nanowire Platforms Suitable for Scalable Production. *ACS Appl. Nano Mater.* **5**, 9063–9071 (2022).

42. Kandziolka, M. *et al.* Silicon nanopillars as a platform for enhanced fluorescence analysis. *Anal. Chem.* **85**, 9031–9038 (2013).

43. Zhao, X., Alizadeh, M. H. & Reinhard, B. M. Harnessing Leaky Modes for Fluorescence Enhancement in Gold-Tipped Silicon Nanowires. *J. Phys. Chem. C* **120**, 20555–20562 (2016).

44. Frederiksen, R. S. *et al.* Modulation of Fluorescence Signals from Biomolecules along Nanowires Due to Interaction of Light with Oriented Nanostructures. *Nano Lett.* **10**, 45 (2021).

45. Frederiksen, R. S. *et al.* Nanowire-Aperture Probe: Local Enhanced Fluorescence Detection for the Investigation of Live Cells at the Nanoscale. *ACS Photonics* **3**, 1208–1216 (2016).

46. Frederiksen, R. *et al.* Visual Understanding of Light Absorption and Waveguiding in Standing Nanowires with 3D Fluorescence Confocal Microscopy. *ACS Photonics* **4**, 2235–2241 (2017).

47. Guo, M. *et al.* Single-shot super-resolution total internal reflection fluorescence microscopy. *Nat. Methods* **15**, 425–428 (2018).

48. Du, B. *et al.* Diameter-optimized high-order waveguide nanorods for fluorescence enhancement applied in ultrasensitive bioassays. *Nanoscale* **11**, 14322–14329 (2019).

49. Singh, M. *et al.* Ultratrace level determination and quantitative analysis of kidney injury biomarkers in patient samples attained by zinc oxide nanorods. *Nanoscale* **8**, 4613–4622 (2016).

50. Kim, J. *et al.* ZnO Nanowire-Based Early Detection of SARS-CoV-2 Antibody Responses in Asymptomatic Patients with COVID-19. *Adv. Mater. Interfaces* **9**, 2102046 (2022).

51. Verardo, D. *et al.* Nanowires for Biosensing: Lightguiding of Fluorescence as a Function of Diameter and Wavelength. *Nano Lett* **18**, 4796–4802 (2018).

52. Kuo, Y.-A. *et al.* Massively Parallel Selection of NanoCluster Beacons. *Adv. Mater.* **34**, 2204957 (2022).

53. Obliosca, J. M. *et al.* A complementary palette of NanoCluster Beacons. *ACS Nano* **8**, 10150–10160 (2014).

54. Schultz, D. *et al.* Structural insights into DNA-stabilized silver clusters. *Soft Matter* **15**, 4284–4293 (2019).

55. Swasey, S. M., Leal, L. E., Lopez-Acevedo, O., Pavlovich, J. & Gwinn, E. G. Silver (I) as DNA glue: Ag+-mediated guanine pairing revealed by removing Watson-Crick constraints. *Sci. Rep.* **5**, 1–9 (2015).

56. Yeh, H. C., Sharma, J., Han, J. J., Martinez, J. S. & Werner, J. H. A DNA-silver nanocluster probe that fluoresces upon hybridization. *Nano Lett.* **10**, 3106–3110 (2010).

57. Shrivastava, S., Triet, N. M., Son, Y. M., Lee, W. I. & Lee, N. E. Seesawed fluorescence nano-aptasensor based on highly vertical ZnO nanorods and three-dimensional quantitative fluorescence imaging for enhanced detection accuracy of ATP. *Biosens. Bioelectron.* **90**, 450–458 (2017).

58. Schaufele, F., Demarco, I. & Day, R. N. FRET Imaging in the Wide-Field Microscope. in *Molecular Imaging* (eds. Periasamy, A. & Day, R. N.) 72–94 (Elsevier Inc., 2005). doi:10.1016/B978-019517720-6.50013-4.

59. Arkin, M. R., Glicksman, M. A., Fu, H., Havel, J. J. & Du, Y. *Inhibition of Protein-Protein Interactions: Non-Cellular Assay Formats*. *Assay Guidance Manual* (Bethesda (MD): Eli Lilly & Company and the National Center for Advancing Translational Sciences, 2004).

60. Michelotti, N., de Silva, C., Johnson-Buck, A. E., Manzo, A. J. & Walter, N. G. A Bird's Eye View. Tracking Slow Nanometer-Scale Movements of Single Molecular Nano-assemblies. *Methods Enzymol.* **475**, 121–148 (2010).

61. Yildiz, A. *et al.* Myosin V walks hand-over-hand: Single fluorophore imaging with 1.5-nm localization. *Science* **300**, 2061–2065 (2003).

62. Von Delius, M. & Leigh, D. A. Walking molecules. *Chem Soc Rev* **40**, 3656–3676 (2011).

63. Rice, S. *et al.* A structural change in the kinesin motor protein that drives motility. *Nature* **402**, 778–784 (1999).

64. Liu, M. *et al.* Biomimetic Autonomous Enzymatic Nanowalker of High Fuel Efficiency. *ACS Nano* **10**, 5882–5890 (2016).

65. Jumper, J. *et al.* Highly accurate protein structure prediction with AlphaFold. *Nature* **596**, 583–589 (2021).

66. Kirkness, M. W. H., Korosec, C. S. & Forde, N. R. Modified Pluronic F127 Surface for Bioconjugation and Blocking Nonspecific Adsorption of Microspheres and Biomacromolecules. *Langmuir* **34**, 13550–13557 (2018).

67. Korosec, C. S., Sivak, D. A. & Forde, N. R. Apparent superballistic dynamics in one-dimensional random walks with biased detachment. *Phys. Rev. Res.* **2**, 033520 (2020).

68. Hu, L., Vecchiarelli, A. G., Mizuuchi, K., Neuman, K. C. & Liu, J. Directed and persistent movement arises from mechanochemistry of the ParA / ParB system. *PNAS* **112**, E7055--E7064 (2015).

69. Bakalar, M. H. *et al.* Size-Dependent Segregation Controls Macrophage Phagocytosis of Antibody-Opsonized Targets. *Cell* **174**, 131-142.e13 (2018).

70. Bui, H. *et al.* Programmable periodicity of quantum dot arrays with DNA origami nanotubes. *Nano Lett.* **10**, 3367–3372 (2010).

71. Messing, M. E., Dick, K. A., Wallenberg, L. R. & Deppert, K. Generation of size-selected gold nanoparticles by spark discharge — for growth of epitaxial nanowires. *Gold Bull.* **42**, 20–26 (2009).

72. Abb, M., Strudley, T., Venn, P., Bakkers, E. P. A. M. & Muskens, O. L. Ultrafast active control of optical transmission pseudomodes in a multiple scattering nanowire layer. in *Active Photonic Materials IV* vol. 8095 102–108 (SPIE, 2011).

73. Marquardt, A., Breitung, E., Weisser, T., Gates, G. & Phaneuf, R. Protecting silver cultural heritage objects with atomic layer deposited corrosion barriers. *Herit. Sci.* **3**, (2015).

74. Deng, L., Kitova, E. N. & Klassen, J. S. Dissociation Kinetics of the Streptavidin–Biotin Interaction Measured Using Direct Electrospray Ionization Mass Spectrometry Analysis. *J. Am. Soc. Mass Spectrom.* **24**, 49–56 (2013).

75. Fukuzaki, S., Urano, H. & Nagata, K. Adsorption of bovine serum albumin onto metal oxide surfaces. *J. Ferment. Bioeng.* **81**, 163–167 (1996).

76. Hu, W., Liu, Y., Zhu, Z., Yang, H. & Li, C. M. Randomly oriented ZnO nanorods as advanced substrate for high-performance protein microarrays. *ACS Appl. Mater. Interfaces* **2**, 1569–1572 (2010).

77. Wang, T. *et al.* Tuneable fluorescence enhancement of nanostructured ZnO arrays with controlled morphology. *Phys. Chem. Chem. Phys.* **20**, 14828–14834 (2018).

78. Verardo, D. *et al.* Fluorescence Signal Enhancement in Antibody Microarrays Using Lightguiding Nanowires. *Nanomater Basel Switz.* **11**, 227 (2021).

79. Anttu, N. *et al.* Geometry Tailoring of Emission from Semiconductor Nanowires and Nanocones. *Photonics* **7**, 23 (2020).

80. Grzela, G. *et al.* Nanowire antenna emission. *Nano Lett.* **12**, 5481–5486 (2012).

81. Van Dam, D. *et al.* Directional and Polarized Emission from Nanowire Arrays. *Nano Lett.* **15**, 4557–4563 (2015).

82. Gu, Z., Song, Q. & Xiao, S. Nanowire Waveguides and Lasers: Advances and Opportunities in Photonic Circuits. *Front. Chem.* **8**, 613504 (2021).

83. Liu, X., Hu, R., Gao, Z. & Shao, N. Photoluminescence Mechanism of DNA-Templated Silver Nanoclusters: Coupling between Surface Plasmon and Emitter and Sensing of Lysozyme. *Langmuir* **31**, 5859–5867 (2015).

84. Yeh, H.-C. *et al.* A Fluorescence Light-Up Ag Nanocluster Probe That Discriminates Single-Nucleotide Variants by Emission Color. *J Am Chem Soc* **134**, 40 (2012).

85. Zhao, X., Wang, S., Zou, R., Chen, C. & Cai, C. An enzyme-free probe based on G-triplex assisted by silver nanocluster pairs for sensitive detection of microRNA-21. *Microchim. Acta* **188**, (2021).

86. Sharma, J., Yeh, H. C., Yoo, H., Werner, J. H. & Martinez, J. S. Silver nanocluster aptamers: in situ generation of intrinsically fluorescent recognition ligands for protein detection. *Chem. Commun.* **47**, 2294–2296 (2011).

87. Aspnes, D. E. & Studna, A. A. Dielectric functions and optical parameters of Si, Ge, GaP, GaAs, GaSb, InP, InAs, and InSb from 1.5 to 6.0 eV. *Phys. Rev. B* **27**, 985–1009 (1983).

88. Charafeddine, R. A., Nosanchuk, J. D. & Sharp, D. J. Targeting Microtubules for Wound Repair. *Adv. Wound Care* **5**, 444–454 (2016).

89. Nicolau Jr., D. V. *et al.* Parallel computation with molecular-motor-propelled agents in nanofabricated networks. *Proc Natl Acad Sci U A* **113**, 2591–2596 (2016).

90. Eilers, Y., Ta, H., Gwosch, K. C., Balzarotti, F. & Hell, S. W. MINFLUX monitors rapid molecular jumps with superior spatiotemporal resolution. *Proc. Natl. Acad. Sci.* **115**, 6117–6122 (2018).

91. Schmidt, R. *et al.* MINFLUX nanometer-scale 3D imaging and microsecond-range tracking on a common fluorescence microscope. *Nat. Commun.* **12**, 1–12 (2021).

92. Copp, S. M., Schultz, D., Swasey, S. M., Faris, A. & Gwinn, E. G. Cluster Plasmonics: Dielectric and Shape Effects on DNA-Stabilized Silver Clusters. *Nano Lett.* **16**, 3594–3599 (2016).

93. Wu, Q. *et al.* Plasmon Coupling in DNA-Assembled Silver Nanoclusters. *J. Am. Chem. Soc.* **143**, 14573–14580 (2021).

94. Pescaglini, A. & Iacopino, D. Metal nanoparticle-semiconductor nanowire hybrid nanostructures for plasmon-enhanced optoelectronics and sensing. *J Mater Chem C* **3**, 11785 (2015).

95. Chen, J. *et al.* Surface-enhanced Raman scattering of rhodamine 6G on nanowire arrays decorated with gold nanoparticles. *Nanotechnology* **19**, 275712 (2008).

96. Heurlin, M. *et al.* Continuous gas-phase synthesis of nanowires with tunable properties. *Nature* **492**, 90–94 (2012).
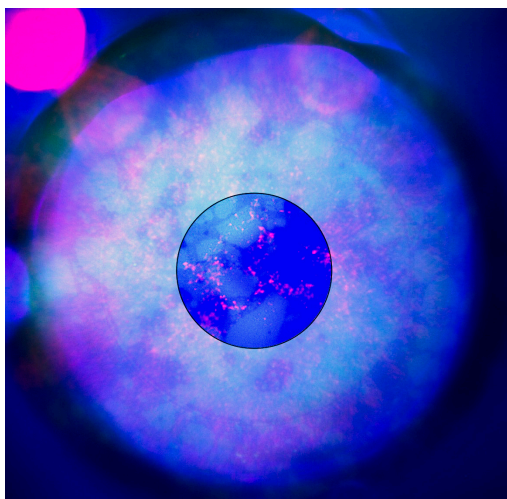
In this thesis, nanowires are used to enhance fluorescence, and now you can look into their eye! This area ended up under a bubble in solution, through which the nanowire fluorescent tips are shining (in magenta pseudo color). The contrast in the center was increased for better visibility.

Faculty of Engineering
Department of Physics
Division of Solid State Physics

ISBN 978-91-8039-802-2